

NASA CR-54176

Cosmic, Inc. Report No. 82

DEVELOPMENT OF A CHARGED COLLOID SOURCE FOR ELECTROSTATIC PROPULSION

by

D. Gignoux, H. F. Anton, and J. J. Shea

prepared for

NATIONAL AERONAUTICS AND SPACE ADMINISTRATION

Contract NAS3-4106

STAGILITY FORM 602

(ACCESSION NUMBER)
75

(PAGES)
1-2-3-4-5-6-7-8-9-10-11-12-13-14-15-16-17-18-19-20-21-22-23-24-25-26-27-28-29-30-31-32-33-34-35-36-37-38-39-40-41-42-43-44-45-46-47-48-49-50-51-52-53-54-55-56-57-58-59-60-61-62-63-64-65-66-67-68-69-70-71-72-73-74-75-76-77-78-79-80-81-82-83-84-85-86-87-88-89-90-91-92-93-94-95-96-97-98-99-100-101-102-103-104-105-106-107-108-109-110-111-112-113-114-115-116-117-118-119-120-121-122-123-124-125-126-127-128-129-130-131-132-133-134-135-136-137-138-139-140-141-142-143-144-145-146-147-148-149-150-151-152-153-154-155-156-157-158-159-160-161-162-163-164-165-166-167-168-169-170-171-172-173-174-175-176-177-178-179-180-181-182-183-184-185-186-187-188-189-190-191-192-193-194-195-196-197-198-199-200-201-202-203-204-205-206-207-208-209-210-211-212-213-214-215-216-217-218-219-220-221-222-223-224-225-226-227-228-229-230-231-232-233-234-235-236-237-238-239-240-241-242-243-244-245-246-247-248-249-250-251-252-253-254-255-256-257-258-259-260-261-262-263-264-265-266-267-268-269-270-271-272-273-274-275-276-277-278-279-280-281-282-283-284-285-286-287-288-289-290-291-292-293-294-295-296-297-298-299-300-301-302-303-304-305-306-307-308-309-310-311-312-313-314-315-316-317-318-319-320-321-322-323-324-325-326-327-328-329-330-331-332-333-334-335-336-337-338-339-340-341-342-343-344-345-346-347-348-349-350-351-352-353-354-355-356-357-358-359-360-361-362-363-364-365-366-367-368-369-370-371-372-373-374-375-376-377-378-379-380-381-382-383-384-385-386-387-388-389-390-391-392-393-394-395-396-397-398-399-400-401-402-403-404-405-406-407-408-409-410-411-412-413-414-415-416-417-418-419-420-421-422-423-424-425-426-427-428-429-430-431-432-433-434-435-436-437-438-439-440-441-442-443-444-445-446-447-448-449-450-451-452-453-454-455-456-457-458-459-460-461-462-463-464-465-466-467-468-469-470-471-472-473-474-475-476-477-478-479-480-481-482-483-484-485-486-487-488-489-490-491-492-493-494-495-496-497-498-499-500-501-502-503-504-505-506-507-508-509-510-511-512-513-514-515-516-517-518-519-520-521-522-523-524-525-526-527-528-529-530-531-532-533-534-535-536-537-538-539-540-541-542-543-544-545-546-547-548-549-550-551-552-553-554-555-556-557-558-559-560-561-562-563-564-565-566-567-568-569-570-571-572-573-574-575-576-577-578-579-580-581-582-583-584-585-586-587-588-589-590-591-592-593-594-595-596-597-598-599-600-601-602-603-604-605-606-607-608-609-610-611-612-613-614-615-616-617-618-619-620-621-622-623-624-625-626-627-628-629-630-631-632-633-634-635-636-637-638-639-640-641-642-643-644-645-646-647-648-649-650-651-652-653-654-655-656-657-658-659-660-661-662-663-664-665-666-667-668-669-670-671-672-673-674-675-676-677-678-679-680-681-682-683-684-685-686-687-688-689-690-691-692-693-694-695-696-697-698-699-700-701-702-703-704-705-706-707-708-709-710-711-712-713-714-715-716-717-718-719-720-721-722-723-724-725-726-727-728-729-730-731-732-733-734-735-736-737-738-739-740-741-742-743-744-745-746-747-748-749-750-751-752-753-754-755-756-757-758-759-760-761-762-763-764-765-766-767-768-769-770-771-772-773-774-775-776-777-778-779-780-781-782-783-784-785-786-787-788-789-790-791-792-793-794-795-796-797-798-799-800-801-802-803-804-805-806-807-808-809-810-811-812-813-814-815-816-817-818-819-820-821-822-823-824-825-826-827-828-829-830-831-832-833-834-835-836-837-838-839-840-841-842-843-844-845-846-847-848-849-850-851-852-853-854-855-856-857-858-859-860-861-862-863-864-865-866-867-868-869-870-871-872-873-874-875-876-877-878-879-880-881-882-883-884-885-886-887-888-889-890-891-892-893-894-895-896-897-898-899-900-901-902-903-904-905-906-907-908-909-910-911-912-913-914-915-916-917-918-919-920-921-922-923-924-925-926-927-928-929-930-931-932-933-934-935-936-937-938-939-940-941-942-943-944-945-946-947-948-949-950-951-952-953-954-955-956-957-958-959-960-961-962-963-964-965-966-967-968-969-970-971-972-973-974-975-976-977-978-979-980-981-982-983-984-985-986-987-988-989-990-991-992-993-994-995-996-997-998-999-1000-1001-1002-1003-1004-1005-1006-1007-1008-1009-1010-1011-1012-1013-1014-1015-1016-1017-1018-1019-1020-1021-1022-1023-1024-1025-1026-1027-1028-1029-1030-1031-1032-1033-1034-1035-1036-1037-1038-1039-1040-1041-1042-1043-1044-1045-1046-1047-1048-1049-1050-1051-1052-1053-1054-1055-1056-1057-1058-1059-1060-1061-1062-1063-1064-1065-1066-1067-1068-1069-1070-1071-1072-1073-1074-1075-1076-1077-1078-1079-1080-1081-1082-1083-1084-1085-1086-1087-1088-1089-1090-1091-1092-1093-1094-1095-1096-1097-1098-1099-1100-1101-1102-1103-1104-1105-1106-1107-1108-1109-1110-1111-1112-1113-1114-1115-1116-1117-1118-1119-1120-1121-1122-1123-1124-1125-1126-1127-1128-1129-1130-1131-1132-1133-1134-1135-1136-1137-1138-1139-1140-1141-1142-1143-1144-1145-1146-1147-1148-1149-1150-1151-1152-1153-1154-1155-1156-1157-1158-1159-1160-1161-1162-1163-1164-1165-1166-1167-1168-1169-1170-1171-1172-1173-1174-1175-1176-1177-1178-1179-1180-1181-1182-1183-1184-1185-1186-1187-1188-1189-1190-1191-1192-1193-1194-1195-1196-1197-1198-1199-1200-1201-1202-1203-1204-1205-1206-1207-1208-1209-1210-1211-1212-1213-1214-1215-1216-1217-1218-1219-1220-1221-1222-1223-1224-1225-1226-1227-1228-1229-1230-1231-1232-1233-1234-1235-1236-1237-1238-1239-1240-1241-1242-1243-1244-1245-1246-1247-1248-1249-1250-1251-1252-1253-1254-1255-1256-1257-1258-1259-1260-1261-1262-1263-1264-1265-1266-1267-1268-1269-1270-1271-1272-1273-1274-1275-1276-1277-1278-1279-1280-1281-1282-1283-1284-1285-1286-1287-1288-1289-1290-1291-1292-1293-1294-1295-1296-1297-1298-1299-1300-1301-1302-1303-1304-1305-1306-1307-1308-1309-1310-1311-1312-1313-1314-1315-1316-1317-1318-1319-1320-1321-1322-1323-1324-1325-1326-1327-1328-1329-1330-1331-1332-1333-1334-1335-1336-1337-1338-1339-1340-1341-1342-1343-1344-1345-1346-1347-1348-1349-1350-1351-1352-1353-1354-1355-1356-1357-1358-1359-1360-1361-1362-1363-1364-1365-1366-1367-1368-1369-1370-1371-1372-1373-1374-1375-1376-1377-1378-1379-1380-1381-1382-1383-1384-1385-1386-1387-1388-1389-1390-1391-1392-1393-1394-1395-1396-1397-1398-1399-1400-1401-1402-1403-1404-1405-1406-1407-1408-1409-1410-1411-1412-1413-1414-1415-1416-1417-1418-1419-1420-1421-1422-1423-1424-1425-1426-1427-1428-1429-1430-1431-1432-1433-1434-1435-1436-1437-1438-1439-1440-1441-1442-1443-1444-1445-1446-1447-1448-1449-1450-1451-1452-1453-1454-1455-1456-1457-1458-1459-1460-1461-1462-1463-1464-1465-1466-1467-1468-1469-1470-1471-1472-1473-1474-1475-1476-1477-1478-1479-1480-1481-1482-1483-1484-1485-1486-1487-1488-1489-1490-1491-1492-1493-1494-1495-1496-1497-1498-1499-1500-1501-1502-1503-1504-1505-1506-1507-1508-1509-1510-1511-1512-1513-1514-1515-1516-1517-1518-1519-1520-1521-1522-1523-1524-1525-1526-1527-1528-1529-1530-1531-1532-1533-1534-1535-1536-1537-1538-1539-1540-1541-1542-1543-1544-1545-1546-1547-1548-1549-1550-1551-1552-1553-1554-1555-1556-1557-1558-1559-1560-1561-1562-1563-1564-1565-1566-1567-1568-1569-1570-1571-1572-1573-1574-1575-1576-1577-1578-1579-1580-1581-1582-1583-1584-1585-1586-1587-1588-1589-1590-1591-1592-1593-1594-1595-1596-1597-1598-1599-1600-1601-1602-1603-1604-1605-1606-1607-1608-1609-1610-1611-1612-1613-1614-1615-1616-1617-1618-1619-1620-1621-1622-1623-1624-1625-1626-1627-1628-1629-1630-1631-1632-1633-1634-1635-1636-1637-1638-1639-1640-1641-1642-1643-1644-1645-1646-1647-1648-1649-1650-1651-1652-1653-1654-1655-1656-1657-1658-1659-1660-1661-1662-1663-1664-1665-1666-1667-1668-1669-1670-1671-1672-1673-1674-1675-1676-1677-1678-1679-1680-1681-1682-1683-1684-1685-1686-1687-1688-1689-1690-1691-1692-1693-1694-1695-1696-1697-1698-1699-1700-1701-1702-1703-1704-1705-1706-1707-1708-1709-1710-1711-1712-1713-1714-1715-1716-1717-1718-1719-1720-1721-1722-1723-1724-1725-1726-1727-1728-1729-1730-1731-1732-1733-1734-1735-1736-1737-1738-1739-1740-1741-1742-1743-1744-1745-1746-1747-1748-1749-1750-1751-1752-1753-1754-1755-1756-1757-1758-1759-1760-1761-1762-1763-1764-1765-1766-1767-1768-1769-1770-1771-1772-1773-1774-1775-1776-1777-1778-1779-1780-1781-1782-1783-1784-1785-1786-1787-1788-1789-1790-1791-1792-1793-1794-1795-1796-1797-1798-1799-1800-1801-1802-1803-1804-1805-1806-1807-1808-1809-1810-1811-1812-1813-1814-1815-1816-1817-1818-1819-1820-1821-1822-1823-1824-1825-1826-1827-1828-1829-1830-1831-1832-1833-1834-1835-1836-1837-1838-1839-1840-1841-1842-1843-1844-1845-1846-1847-1848-1849-1850-1851-1852-1853-1854-1855-1856-1857-1858-1859-1860-1861-1862-1863-1864-1865-1866-1867-1868-1869-1870-1871-1872-1873-1874-1875-1876-1877-1878-1879-1880-1881-1882-1883-1884-1885-1886-1887-1888-1889-1890-1891-1892-1893-1894-1895-1896-1897-1898-1899-1900-1901-1902-1903-1904-1905-1906-1907-1908-1909-1910-1911-1912-1913-1914-1915-1916-1917-1918-1919-1920-1921-1922-1923-1924-1925-1926-1927-1928-1929-1930-1931-1932-1933-1934-1935-1936-1937-1938-1939-1940-1941-1942-1943-1944-1945-1946-1947-1948-1949-1950-1951-1952-1953-1954-1955-1956-1957-1958-1959-1960-1961-1962-1963-1964-1965-1966-1967-1968-1969-1970-1971-1972-1973-1974-1975-1976-1977-1978-1979-1980-1981-1982-1983-1984-1985-1986-1987-1988-1989-1990-1991-1992-1993-1994-1995-1996-1997-1998-1999-2000-2001-2002-2003-2004-2005-2006-2007-2008-2009-2010-2011-2012-2013-2014-2015-2016-2017-2018-2019-2020-2021-2022-2023-2024-2025-2026-2027-2028-2029-2030-2031-2032-2033-2034-2035-2036-2037-2038-2039-2040-2041-2042-2043-2044-2045-2046-2047-2048-2049-2050-2051-2052-2053-2054-2055-2056-2057-2058-2059-2060-2061-2062-2063-2064-2065-2066-2067-2068-2069-2070-2071-2072-2073-2074-2075-2076-2077-2078-2079-2080-2081-2082-2083-2084-2085-2086-2087-2088-2089-2090-2091-2092-2093-2094-2095-2096-2097-2098-2099-2100-2101-2102-2103-2104-2105-2106-2107-2108-2109-2110-2111-2112-2113-2114-2115-2116-2117-2118-2119-2120-2121-2122-2123-2124-2125-2126-2127-2128-2129-2130-2131-2132-2133-2134-2135-2136-2137-2138-2139-2140-2141-2142-2143-2144-2145-2146-2147-2148-2149-2150-2151-2152-2153-2154-2155-2156-2157-2158-2159-2160-2161-2162-2163-2164-2165-2166-2167-2168-2169-2170-2171-2172-2173-2174-2175-2176-2177-2178-2179-2180-2181-2182-2183-2184-2185-2186-2187-2188-2189-2190-2191-2192-2193-2194-2195-2196-2197-2198-2199-2200-2201-2202-2203-2204-2205-2206-2207-2208-2209-2210-2211-2212-2213-2214-2215-2216-2217-2218-2219-2220-2221-2222-2223-2224-2225-2226-2227-2228-2229-2230-2231-2232-2233-2234-2235-2236-2237-2238-2239-2240-2241-2242-2243-2244-2245-2246-2247-2248-2249-2250-2251-2252-2253-2254-2255-2256-2257-2258-2259-2260-2261-2262-2263-2264-2265-2266-2267-2268-2269-2270-2271-2272-2273-2274-2275-2276-2277-2278-2279-2280-2281-2282-2283-2284-2285-2286-2287-2288-2289-2290-2291-2292-2293-2294-2295-2296-2297-2298-2299-2300-2301-2302-2303-2304-2305-2306-2307-2308-2309-2310-2311-2312-2313-2314-2315-2316-2317-2318-2319-2320-2321-2322-2323-2324-2325-2326-2327-2328-2329-2330-2331-2332-2333-2334-2335-2336-2337-2338-2339-2340-2341-2342-2343-2344-2345-2346-2347-2348-2349-2350-2351-2352-2353-2354-2355-2356-2357-2358-2359-2360-2361-2362-2363-2364-2365-2366-2367-2368-2369-2370-2371-2372-2373-2374-2375-2376-2377-2378-2379-2380-2381-2382-2383-2384-2385-2386-2387-2388-2389-2390-2391-2392-2393-2394-2395-2396-2397-2398-2399-2400-2401-2402-2403-2404-2405-2406-2407-2408-2409-2410-2411-2412-2413-2414-2415-2416-2417-2418-2419-2420-2421-2422-2423-2424-2425-2426-2427-2428-2429-2430-2431-2432-2433-2434-2435-2436-2437-2438-2439-2440-2441-2442-2443-2444-2445-2446-2447-2448-2449-2450-2451-2452-2453-2454-2455-2456-2457-2458-2459-2460-2461-2462-2463-2464-2465-2466-2467-2468-2469-2470-2471-2472-2473-2474-2475-2476-2477-2478-2479-2480-2481-2482-2483-2484-2485-2486-2487-2488-2489-2490-2491-2492-2493-2494-2495-2496-2497-2498-2499-2500-2501-2502-2503-2504-2505-2506-2507-2508-2509-2510-2511-2512-2513-2514-2515-2516-2517-2518-2519-2520-2521-2522-2523-2524-2525-2526-2527-2528-2529-2530-2531-2532-2533-2534-2535-2536-2537-2538-2539-2540-2541-2542-2543-2544-2545-2546-2547-2548-2549-2550-2551-2552-2553-2554-2555-2556-2557-2558-2559-2560-2561-2562-2563-2564-2565-2566-2567-2568-2569-2570-2571-2572-2573-2574-2575-2576-2577-2578-2579-2580-2581-2582-2583-2584-2585-2586-2587-2588-2589-2590-2591-2592-2593-2594-2595-2596-259

NASA CR-54176

Cosmic, Inc. Report No. 82

FINAL REPORT

DEVELOPMENT OF A CHARGED
COLLOID SOURCE FOR ELECTROSTATIC PROPULSION

by

D. Gignoux, H. F. Anton, and J. J. Shea

prepared for

NATIONAL AERONAUTICS AND SPACE ADMINISTRATION

October 1964

CONTRACT NAS3-4106

Technical Management
NASA Lewis Research Center
Cleveland, Ohio
Electric Propulsion Office
John Ferrante

COSMIC, INC.
3206 Grace Street, N. W.
Washington, D. C. 20007

TABLE OF CONTENTS

	<u>Page</u>
SUMMARY	ii
LIST OF FIGURES	iii
TABLE OF SYMBOLS	vi
1. INTRODUCTION	1
2. DESCRIPTION OF THE EXPERIMENT	6
2.1 Principle of Operation of the Colloid Source	6
2.2 Propellant Feed System	6
2.3 The Nozzle and Its Drive	8
2.4 The Extractor and Collector Electrodes	8
2.5 Test Facility	10
2.6 Measuring Instruments	13
2.7 Massenfilter	15
3. THEORETICAL ANALYSIS OF SYSTEM PERFORMANCE	23
4. CHEMICAL INVESTIGATIONS	38
5. TESTS OF PROPELLANTS AND GEOMETRIES	46
5.1 Test Procedure	46
5.2 Tests with Liquid Metals	47
5.3 Tests with Organic Propellants	49
5.4 Tests with Polyphosphoric Acid	49
5.5 Tests with Massenfilter	54
6. RESULTS AND INTERPRETATION OF PERFORMANCE MAPPING EXPERIMENTS	56
7. CONCLUSIONS AND RECOMMENDATIONS	67
REFERENCES	68
DISTRIBUTION LIST	69
ABSTRACT	73

SUMMARY

15876

A large number of tests have been performed with a rotating nozzle source of induction charged colloid.

The geometry has been improved resulting in an increase of the charge-to-mass ratio by one order of magnitude with respect to a previous program. Analytically, the ideal propellant has been shown to have high viscosity, low density, low surface tension, low vapor pressure, and high conductivity. The experimental values of the system parameters agreed conclusively with those predicted analytically. The search for a better propellant has disclosed several promising avenues. Beam currents up to 1.5 milliamperes have been obtained. The system has very promising application to high efficiency electrostatic thrusters.

Burton

LIST OF FIGURES

<u>Figure Number</u>	<u>Title</u>	<u>Page</u>
1	Efficiency of Ion Engines (after Mickelsen and Kaufman)	1
2	Principle of Operation of the Spinning Nozzle Colloid	5
3	Propellant Feed System	7
4	Back Plate of Test Chamber with Nozzle Drive and High Voltage Bushing	7
5	Five Nozzles	9
6	10° Nozzle, Bearing Block, and Insulation Mounting	9
7	The Nozzle Drive Assembly	10
8	Several Extractors and One Collector	11
9	Overall View of Test Facility	12
10	Inside View of Vacuum Chamber	13
11	Schematic of Instrumentation	14
12	Thrust Measuring System	14
13	Typical Recordings of Voltage and Microbalance Output	16
14	Massenfilter Quadrupole.	21
15	End Plate of Test Chamber with Adjustable Quadrupole	21
16	Schematic Diagram. Audio Frequency and DC Power Supply, Mass Spectrometer	22
17	The Functions $j = H(e_o)$ and $e_o = K(j)$, Relating Dimensionless Source Field, e_o , and Dimensionless Current Density, j , for Space Charge Flow Between Parallel Planes	28
18	The Function $g_1(x)$ Defined by Space-Charge Flow Between Parallel Planes	29

<u>Figure Number</u>	<u>Title</u>	<u>Page</u>
19	Nomogram for Efficiency Calculations	48
20	Propellant Tests, Beam Current vs. Accelerating Voltage	50
21	Propellant Tests, Beam Current vs. Accelerating Voltage	50
22	Propellant Tests, Beam Current vs. Accelerating Voltage	51
23	Propellant Tests, Beam Current vs. Accelerating Voltage	51
24	Average Charge-to-Mass Ratio (q/m), Total Thrust per Mass Flow (F_T/\dot{m}) and Efficiency (η) vs. Accelerating Voltage	52
25	Average Charge-to-Mass Ratio vs. Accelerating Voltage for Various Nozzle-Extractor Distances	53
26	Average Charge-to-Mass Ratio vs. Accelerating Voltage for Various Nozzle-Extractor Distances (Log-Log Scale).	53
27	Massenfilter Current vs. Charge-to-Mass Ratios	55
28	Equivalent Collector Current vs. Voltage for a Rotating Speed of 5,000 rpm and Total Mass Flow Rates of 0.5, 3, and 15×10^{-6} kg/sec.	59
29	Equivalent Target Current vs. Voltage for a Rotating Speed of 5,000 rpm and Total Mass Flow Rates of 0.5, 3, and 15×10^{-6} kg/sec.	59
30	Equivalent Target Thrust vs. Voltage for a Rotating Speed of 5,000 rpm and Total Mass Flow Rates of 0.5, 3, and 15×10^{-6} kg/sec.	60
31	Equivalent Collector Current vs. Voltage for a Total Mass Flow of 0.5×10^{-6} kg/sec and Rotating Speeds of 1,000, 5,000 and 12,000 rpm	60
32	Equivalent Target Current vs. Voltage for a Total Mass Flow of 0.5×10^{-6} kg/sec and Rotating Speeds of 1,000, 5,000 and 12,000 rpm	61

<u>Figure Number</u>	<u>Title</u>	<u>Page</u>
33	Equivalent Target Thrust vs. Voltage for a Total Mass Flow of 0.5×10^{-6} kg/sec and Rotating Speeds of 1,000, 5,000 and 12,000 rpm	61
34	Equivalent Target Current vs. Rotating Speed for a Total Mass Flow Rate of 3×10^{-6} kg/sec and Voltage of 24, 30, and 34 KV	62
35	Equivalent Target Thrust vs. Rotating Speed for a Total Mass Flow Rate of 3×10^{-6} kg/sec and Voltage of 24, 30, and 34 KV	62
36	Equivalent Target Current vs. Target Mass Flow Rate for a Voltage of 20 KV and Rotating Speeds of 1,000, 5,000 and 12,000 rpm	63
37	Equivalent Target Thrust vs. Target Mass Flow Rate for a Voltage of 20 KV and Rotating Speeds of 1,000, 5,000 and 12,000 rpm	63
38	Equivalent Target Thrust vs. Target Mass Flow Rate for a Rotating Speed of 5,000 rpm and Voltage of 20, 30, 37 KV	65
39	Rayleigh Maximum Specific Charge as a Function of Drop Sizes	65

LIST OF SYMBOLS

<u>Symbol</u>	<u>Definition</u>	<u>Dimension</u>
a	characteristic size of droplet	L
b	radius of quadrupole rails	l
d	radius of quadrupole	L
e _o	normalized electric field at source	1
f	frequency	1/T
f _n , g _n	dimensionless functions defined by space-charge flow	1
h	film thickness	L
j	normalized current density	1
l	characteristic length of electrode system	
m	mass of droplet	M
\dot{m}	mass flow rate	M/T
q	charge of droplet	Q
r	radius of nozzle	L
s	electrode separation in parallel plane geometry	L
v	exhaust velocity of droplet	L/T
A	emissive area	L ²
B	dimensionless constant in expression for space-charge limit	1
C _{1, 3}	dimensionless constants in expressions for charge-to-mass ratio	1
D	dimensionless constant in expression for film thickness	1
E	electric field	ML/T ² Q
F	thrust of beam	ML/T ²
G	coefficient in Mathieu equation	1
H	dimensionless function determined by space-charge flow	1
J	current density of beam	Q/L ² T
K	dimensionless function determined by space-charge flow	1
K _{1, 2, 3, 4}	dimensionless constants in expressions for charge-to-mass ratio	1
L	distance between nozzle and extractor electrode	L
P	power of beam	ML ² /T ² Q
T	temperature	Θ
V	voltage	ML ² /T ² Q

<u>Symbol</u>	<u>Definition</u>	<u>Dimension</u>
γ	surface tension of propellant	M/T^2
ϵ	capacitivity	$T^2 Q^2 / ML^3$
λ	dimensionless parameter depending on controllable elements	1
μ	dimensionless parameter depending on controllable elements	1
ν	kinematic viscosity	L^2/T
ρ	resistivity of propellant	ML^3/TQ^2
ρ_m	mass density of propellant	M/L^3
σ	conductivity of propellant	TQ^2/ML^3
τ	characteristic time available for charging droplet	T
ω	angular velocity of nozzle	$1/T$
Γ	dimensionless parameter depending on controllable elements	1

1. INTRODUCTION

This is a report on the work accomplished at Cosmic, Inc. during the period September 1963 to September 1964 on a charged colloid generating system for electric propulsion.

To travel long distances through space will require engines with a moderate consumption of propellants. One of the performance parameters utilized to describe propulsion systems is the specific impulse, which is defined as the ratio of the thrust to the weight of propellant consumed per second and is expressed in seconds. It is also known, on the other hand, that the production of a given thrust will require a higher amount of power for a high value of the specific impulse. We will define later on in this report a parameter, the efficiency, representing the utilization of power.

The most promising of the high specific impulse thrustors are the electrostatic thrustors, the best known of which are the ion engines currently in the stage of advanced development. However, ion engines all exhibit the same characteristics, i.e., their efficiency is lower for lower values of the specific impulse. In Figure 1, taken from Reference 1, the efficiency of various thrustors as a function of specific impulse is plotted.

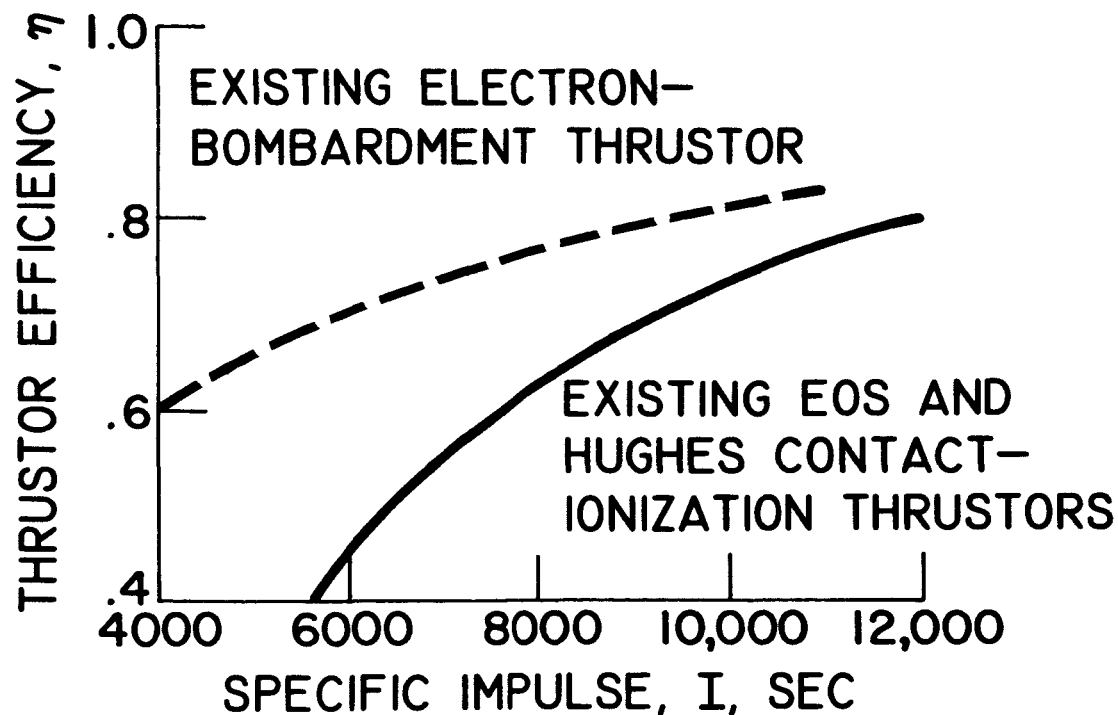


Figure 1. Efficiency of Ion Engines (after Mickelsen and Kaufman).

This figure clearly shows that in the low specific impulse range, there is a need for thrusters capable of high efficiency. Engines using colloid particles, sometimes referred to as heavy particles, seem capable of filling this need. Another limitation of the ion engine is that the current density in an electrostatic accelerator is limited by space charge effects as expressed by the Child-Langmuir law. Consequently, to reach high values of the thrust, a substantial emitting surface must be used to accommodate a large ion current. On the other hand, with colloid particles, the same thrust can be obtained by accelerating the particles to a high voltage. The beam current is relatively low, thereby permitting a smaller emitting surface. For the purposes of this introduction, these qualitative considerations suffice; a quantitative discussion is given in Reference 2.

The "prehistoric" space propulsion thinkers such as Goddard and Oberth seem to have considered ions as the only possibility for electric propulsion. However, when electric propulsion became "legitimate", the advantages of colloid particles, which have been mentioned above, became immediately apparent. Solid particles charged by contact (Reference 3) were first considered but were abandoned in view of the difficulties encountered in charging them. Liquids or condensation sources were found more practical. The charged colloid sources currently under development are of two kinds, depending on whether the particles are charged by induction or by a corona discharge. In the induction charging method, a liquid drop is formed at an edge or at the tip of a needle. If the liquid is conducting, it acts as one electrode of a system of two electrodes, the other being an accelerating electrode at a high potential with respect to the liquid. In this manner, electric charges migrate through the conducting liquid to its surface, the surface of the liquid is submitted to an electrostatic pressure, and the droplet is eventually detached while keeping its surface electric charge. In the corona charging system, a fluid is caused to condense into small solid or liquid particles within an area which is submitted to an intense electron bombardment.

Numerous experiments have been made with liquid being charged by induction at the tip of hollow needles: the liquid moves through the body of the needle and forms cusps attached to the circular edge at the end of the needle. These experiments have proved that charging by induction is feasible and that reasonably narrow distributions of the charge-to-mass ratio of the liquid particles can be obtained. The results obtained for one needle and even the results obtained with an array of 37 needles (Reference 4) correspond to very small values of the beam current and of the thrust. In fact, experimenters with needles have limited themselves to explorations of the beam and measurements of the charge and charge-to-mass ratio of single particles and have not measured the overall

thrust produced by the colloid beam. Table I compares the results obtained by various experimenters in the past year.

In the system utilized at Cosmic, Inc. colloid particles are produced along the circumference of a spinning conical nozzle (Figure 2). In this manner, much higher values of the beam current and mass flow are obtained, a substantial thrust can be measured, and full accountability of the currents and mass flows is possible. In a first effort (Reference 5), a charged colloid source was built at Cosmic, Inc. and preliminary experiments demonstrated that this source could produce charged colloid beams with substantial currents and thrusts. In a second effort, which will be reported herein, a new test facility has been built, and a better geometry has made it possible to obtain a higher thrust and higher charge-to-mass ratio of the particles. In this report, we shall first describe the charged colloid source, the test station utilized for the experiments, and the theoretical investigations of system performance, then summarize the chemical investigation undertaken in the search for better propellants, and finally, present the experimental data and compare them with the results of the theoretical analysis.

TABLE I. Summary of Current Data on Colloid Experiments

Experi- menter	Type of Emitter	Propellant	Propellant Resisti- vity Ohm-Cm	q/m Coul/Kgm	Beam Current 10^{-6} Amps	Accelerating Kilo- Voltage	Mass Flow 10^{-6} kg/sec	Thrust Newtons	Remarks
NASA (Norgren, Golden, et al)	condensing throat	HgCl AlCl ₃		50-100 10^3 - $3 \cdot 10^3$	1-6 5-20	10 10			
USAF (Hunter, Wineland)	1 needle .004 to .008 I.D.	Glycerol + NaCl	$5 \cdot 10^3$	500	1-5	20-30			
STL (Cohen)	37 needles	Glycerol + H ₂ SO ₄	$5 \cdot 10^3$	350	135		0.7		65% effi- ciency
Cosmic, Inc.	spinning nozzle	Octoil + TNBAP Polyphos- phoric Acid	10^6 30	50-180 600	up to 1,500 600	10-60 20	.5 to 30 1	10^{-4} to 1.5×10^{-2}	60-80% efficiency Not measured

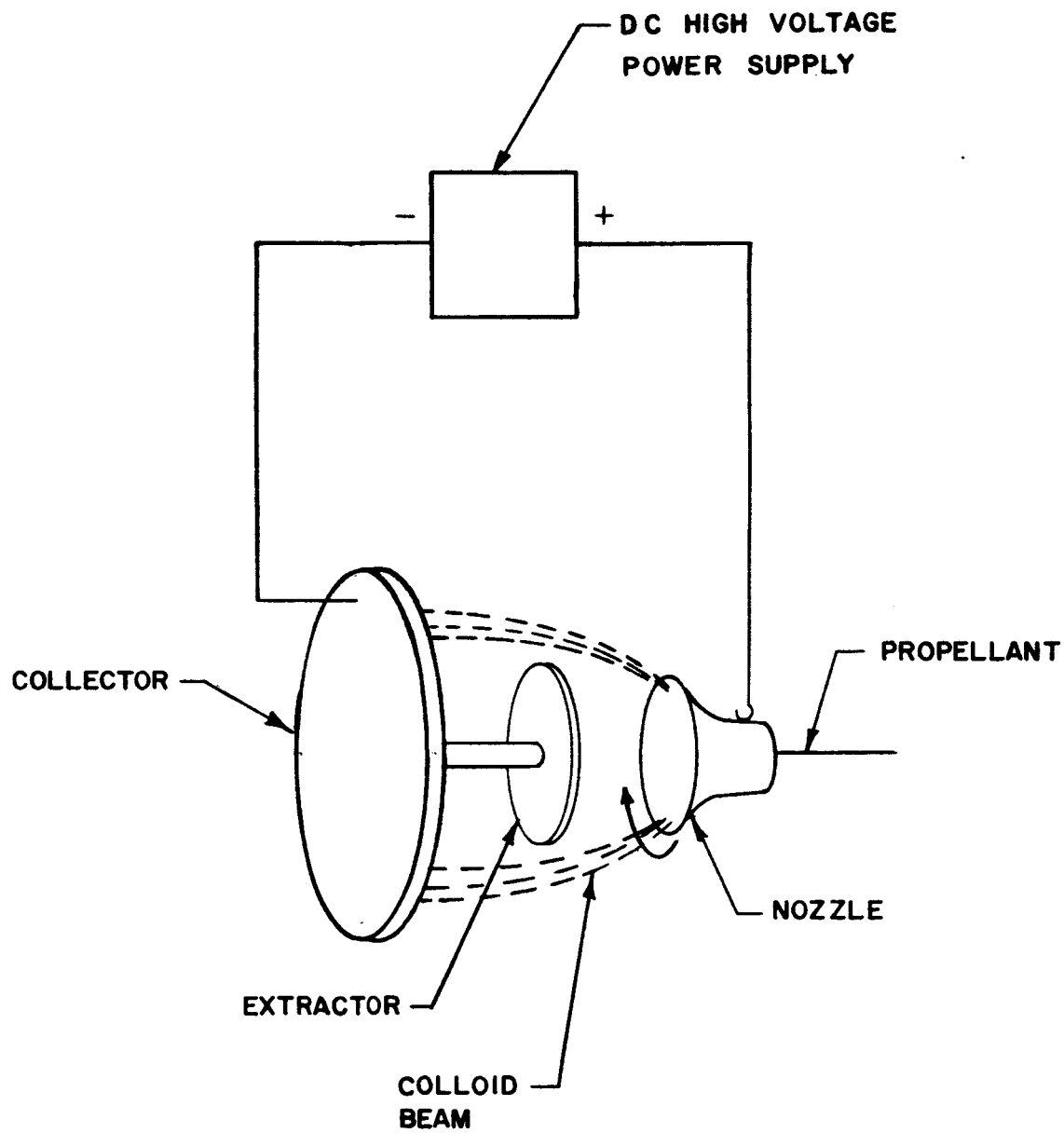


Figure 2. Principle of Operation of the Spinning Nozzle Colloid Source.

2. DESCRIPTION OF THE EXPERIMENT

The test facility consists of a propellant feed system, a rotating nozzle, a system of extracting and collecting electrodes, and instrumentation. These will be described in turn in this chapter.

2.1 Principle of Operation of the Colloid Source

In the colloid source shown in Figure 2, the liquid is injected into the center of a hollow rapidly rotating nozzle. Under the action of the centrifugal force, the liquid expands inside the nozzle to form a thin film which is subjected to the electric field as it reaches the edge of the nozzle. The liquid droplets are pulled off as shown in Figure 2 by the electric field applied by two electrodes: an extractor electrode and a collector electrode. Two configurations of extractor electrodes have been utilized successfully: one consisting of a disc positioned inside the beam (this is the configuration shown in Figure 2) and the other consisting of a ring surrounding the outside of the nozzle. The extractor and collector electrodes are at the same potential. The collector electrode serves primarily for the measurement of beam characteristics. In an actual space thruster system, there would be no collector electrode and the beam would continue its course past the extracting electrode and through a system of accelerating electrodes until neutralized.

2.2 Propellant Feed System

The propellant feed system is shown in Figure 3. It consists of a piston that is driven through a cylinder at a constant velocity by means of a synchronous motor. The piston is insulated so that it can be operated at high voltage. The entire system is mounted on an insulating plate. By changing the synchronous motor, it is possible to vary the mass flow of a propellant having a density of 1000 kilograms per cubic meter as follows: 0.125, 0.25, 0.5, 1.5, 3, 7.5, 15, and 30×10^{-6} kg/sec. The cylinder is recharged from a reservoir.

Great difficulties were encountered with air bubbles in the early experiments, in which the cylinders used were ground precision glass cylinders. Much better results were obtained with ordinary glass tubes. It is felt that ordinary glass tubes have a smoother surface for the O-ring of the piston and therefore make a better seal than the ground glass cylinders. As can be seen in Figure 4, the propellant leaves the cylinder and flows into a stainless steel tube which passes through the center of a high voltage bushing and enters the vacuum enclosure.

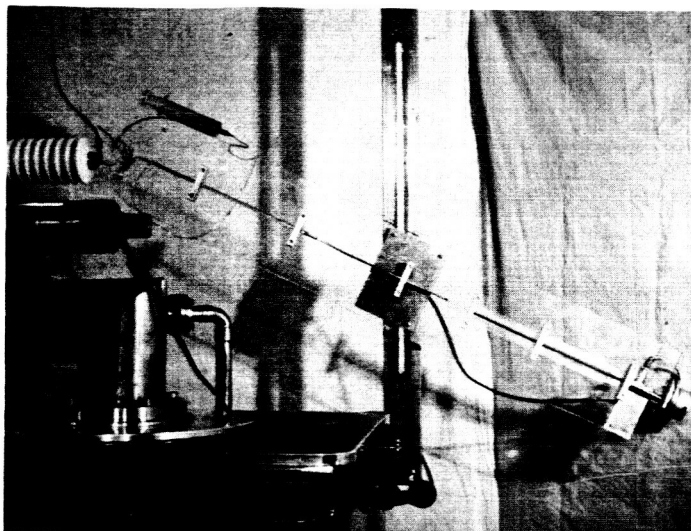


Figure 3. Propellant Feed System

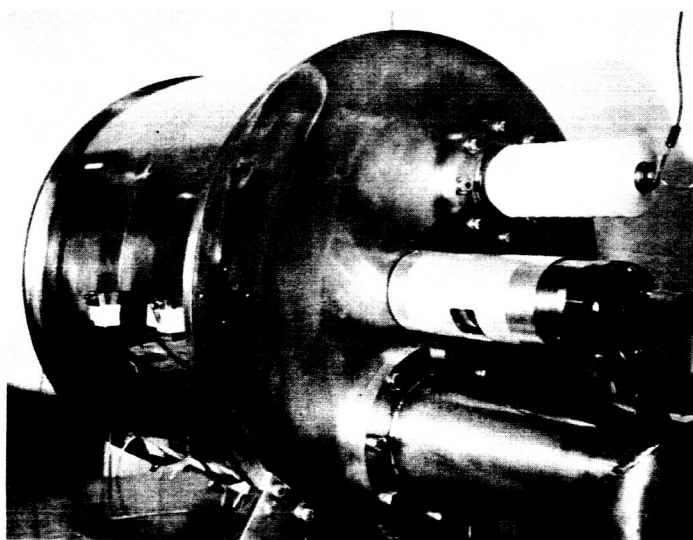


Figure 4. Back Plate of Test Chamber with Nozzle Drive and High Voltage Bushing

2.3 The Nozzle and Its Drive

Several nozzles are shown in Figure 5, and a nozzle assembled on the rotating shaft is shown in Figure 6. The propellant delivery tube ends in a chamber in the back of the nozzle. From this chamber, the liquid flows through a number of holes to the conical chamber forming the front of the nozzle, where it is expanded by the centrifugal force and forms a thin film. With a very low mass flow, the propellant entered the nozzle drop by drop, resulting in a lack of stability in the mass flow in the beam. In the course of the program, this defect was corrected by bringing the end of the tube supplying the propellant to a position very close to the inside surface of the nozzle so that the end of the tube actually dips into the propellant contained in the back part of the nozzle. This resulted in a steady flow of the propellant. Figure 6 shows the nozzle and its bearing block. The bearing block is mounted on four standoff insulators, and the connection of the nozzle shaft to the drive is by means of an insulated coupling. This permits operation of the nozzle at high voltage. The motor drive and the magnetic passthrough are attached to the base plate. The complete assembly of the rotating part: nozzle, bearing, block, coupling, magnetic feedthrough and driving motor is shown in Figure 7. This assembly is the same in principle as that developed under the previous program and described in Reference 6. The magnetic pass-through that transmits the high rotating speed inside the vacuum chamber has, however, been precision balanced, permitting operation without vibration for short durations at 18,000 rpm and continuously at 10,000 rpm. For continuous operation at higher speed, additional cooling would be required. The film flow inside the nozzle was analyzed during a previous investigation (Reference 6). A relationship was found between the mass flow \dot{m} and the film thickness h , and the characteristics of the nozzle. For an ideal nozzle, which would consist of a cone of half angle α the relation is as follows:

$$\dot{m} = (2 \pi / 3) (\sin \alpha) \rho_m^2 r^2 \omega^2 h^3 / \nu,$$

where r and ω are the exit radius and angular velocity, respectively, of the nozzle and ρ_m and ν are the density and viscosity, respectively, of the propellant.

2.4 The Extractor and Collector Electrodes

It is anticipated that in an actual thruster a high accelerating voltage will be required. Since this accelerating voltage cannot be applied to the droplets directly, it will have to be applied in several stages, and it is convenient to call the first stage the extractor electrode. In the



Figure 5. Five Nozzles. The nozzle in the upper left is the one utilized in the performance mapping experiment.

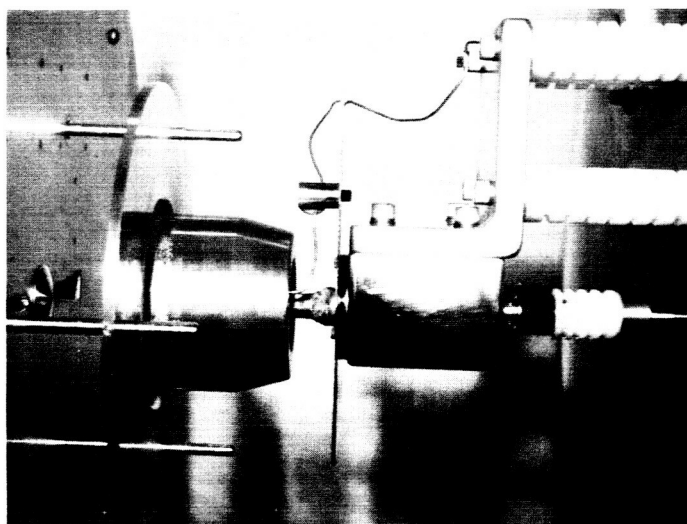


Figure 6. 10° Nozzle, Bearing Block, and Insulation Mounting. The nozzle is shown flush with an annular extractor.

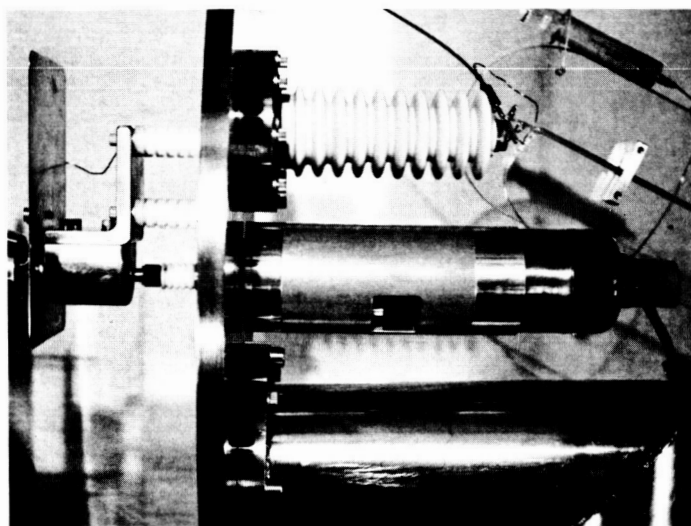


Figure 7. The Nozzle Drive Assembly. The high voltage feedthrough is shown on top, the pumping duct on the bottom.

experiments undertaken here, which are aimed primarily at charging particles and examining the charging mechanism, this first stage alone is used. As mentioned earlier an extractor and an accelerator are used. These two electrodes can be seen clearly in Figure 6. Several types of extractors utilized are shown in Figure 8. They consist of a disc with a diameter smaller than that of the nozzle, a torus with an inner diameter larger than that of the nozzle, or a combination of both. A nozzle utilizing a mesh has also been used.

2.5 Test Facility

An overall view of the test facility is shown in Figure 9. The nozzle, as well as the collector and extractor electrodes are located inside a vacuum chamber which consists of a glass cylinder 20 inches in diameter and 24 inches long. A plexiglass cylinder surrounds the glass cylinder to prevent accidental breakage. The two end plates which close the cylinder are of stainless steel. The end plate shown in Figure 4 is connected to the pumping system. The nozzle drive and the high voltage feedthrough are mounted on this system. The other end plate is mounted on hinges so that the chamber can be opened conveniently for maintenance and cleaning. The extractor and collector electrodes, the balance, and massenfilter are mounted on this end plate. The extractor and collector

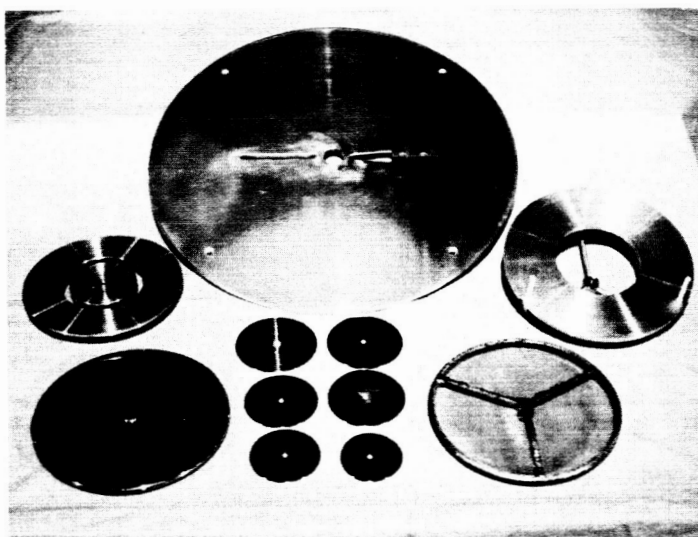


Figure 8. Several Extractors and One Collector. The triangular window on the right of the collector is for thrust measurements, the elongated window on the left for massenfilter analysis.

electrodes are mounted on movable supports. These supports are shown more clearly in Figure 10. The collector is mounted on four insulating sleeves which slide on metal rods. A rotary push-pull feedthrough is located in the center of this end plate. The shaft of the feedthrough makes it possible to adjust the collector and extractor electrodes independently from outside the vacuum chamber.

The propellant feed system is mounted on an insulating plexiglass plate. This plate is so mounted on a rail that it can be inclined at an angle of $\pm 45^\circ$ with respect to the horizontal. This feature helps in keeping the system free of air bubbles. The high voltage power supply is an electrostatic generator of the type originally developed by Cosmic, Inc. and described in Reference 7. This generator is capable of a maximum current of 600 microamperes and a maximum voltage of 80,000 volts, and has a practically negligible internal capacitance. The low internal capacitance means that the generator is not dangerous to the personnel operating it (no special protection is needed) and that a discharge occurring in the vacuum chamber will not result in the release of a large amount of energy. This generator is therefore a great help for operating delicate instrumentation inside the vacuum chamber. A separate control console contains most of the instrumentation, the meters, and a recorder. It will be described in the next section.

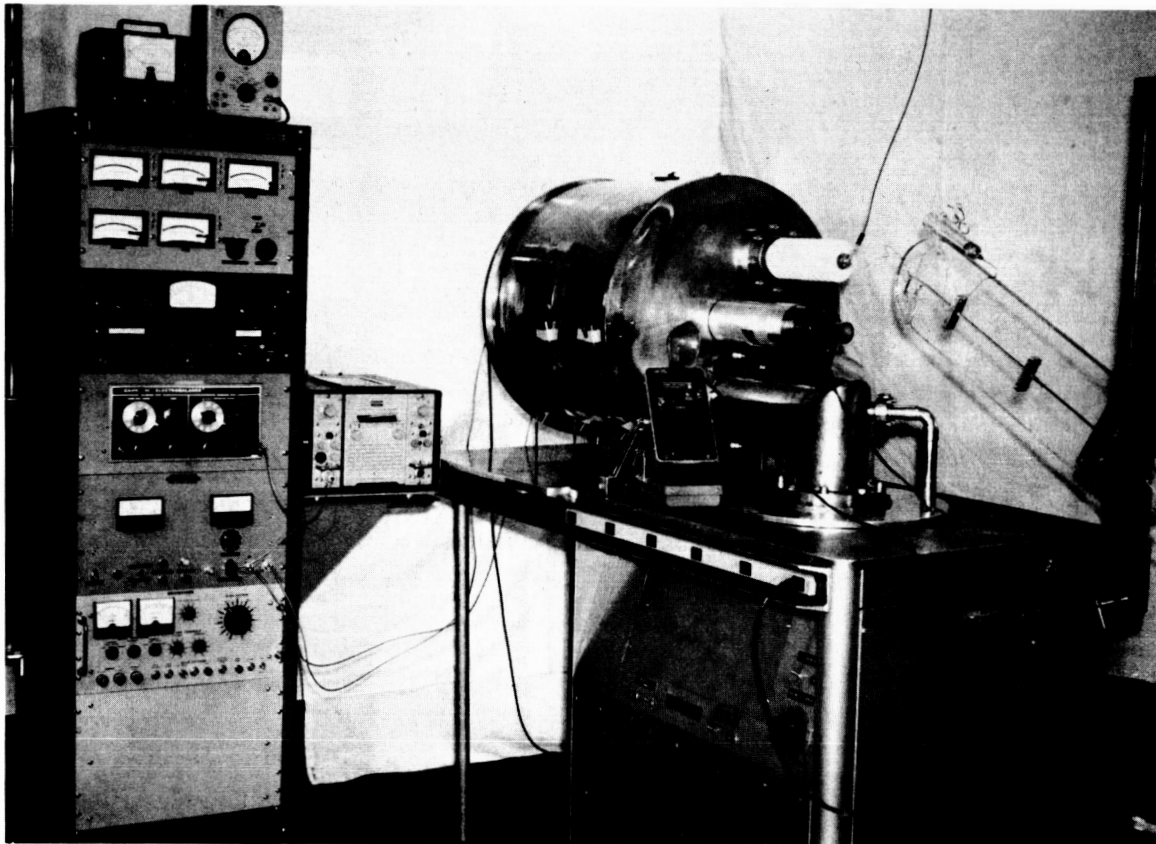


Figure 9. Overall View of Test Facility

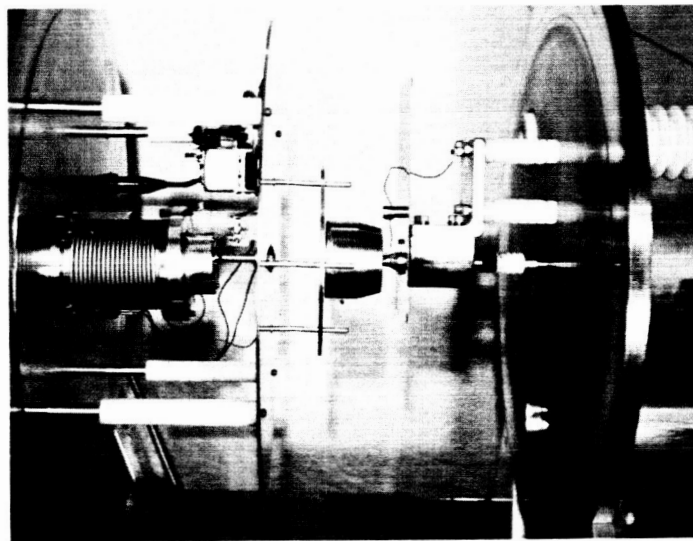


Figure 10. Inside View of Vacuum Chamber

2.6 Measuring Instruments

The instruments used for the measurements are shown in schematic form in Figure 11. For the sake of simplicity, we shall describe the instruments in terms of the measurements which they accomplish. As can be seen in Figure 11, the beam is accelerated toward the collector, and a portion of the beam is sampled through two small windows in the collector for thrust measurement and massenfilter analysis. The following measurements of beam current are effected.

- (a) Ground to nozzle
- (b) Extractor to ground
- (c) Collector to ground
- (d) Thrust measuring target to ground

The high voltage is measured by means of a voltage divider and is constantly recorded during the experiments. The thrust is measured by means of a plate (target) mounted on a pivot point, as shown schematically in Figure 11 and by a photograph in Figure 12. The horizontal force due to the thrust of the colloid beam and the vertical force due to the accumulation of propellant result in a moment which is transmitted to the electro-balance. The measurements are transmitted to the main control console (left in Figure 9) where they are recorded. The plate or target is attached to a shaft in such a manner that the thrust and the force resulting

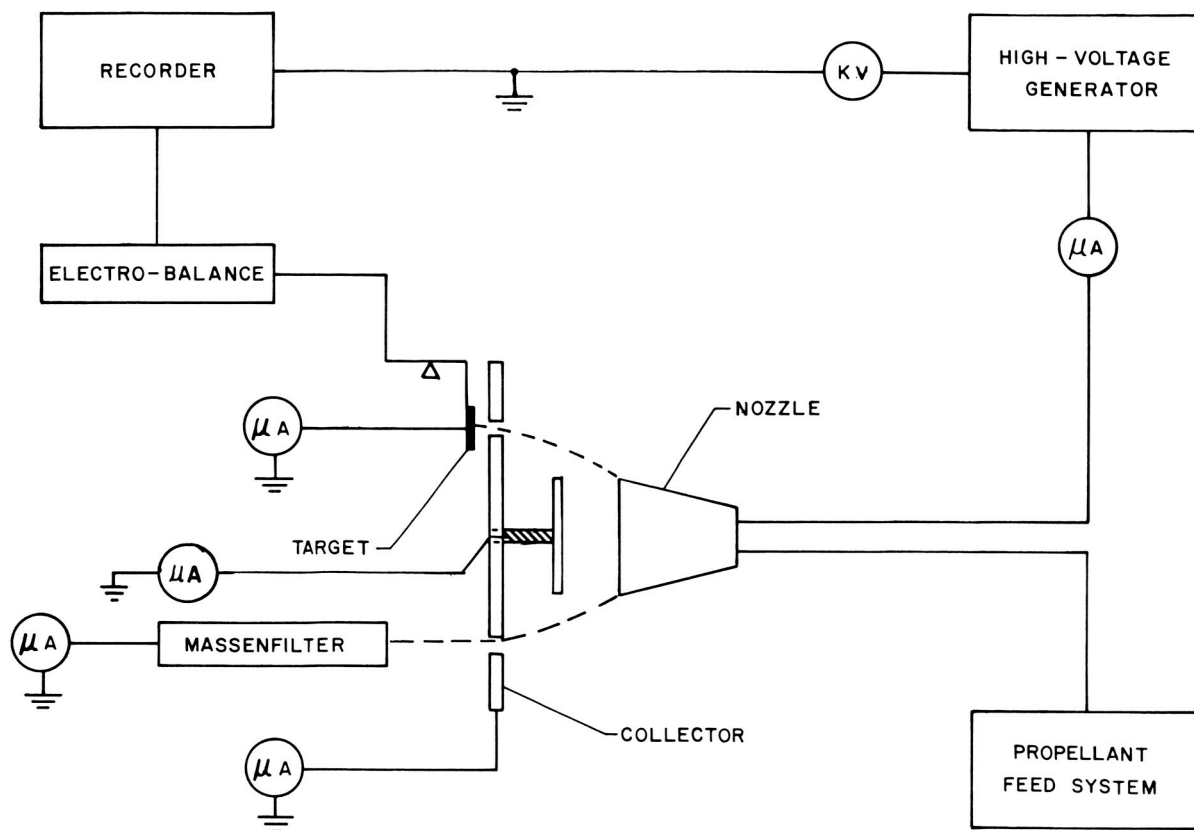


Figure 11. Schematic of Instrumentation

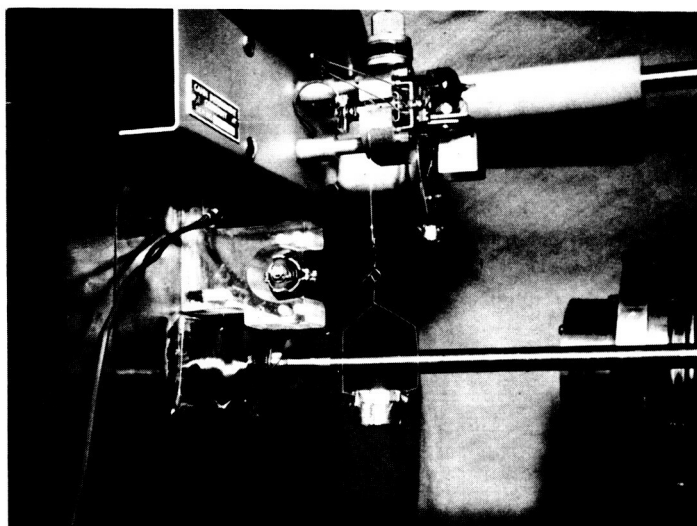


Figure 12. Thrust Measuring System. Showing the rectangular, thrust measuring plate, its pivot and the electrobalance.

from mass accumulation on the target have the same moment with respect to the axis. In this manner, thrust and mass accumulation are added in the indication of the microbalance. The thrust is determined by the difference between the balance indication with the high voltage on and off. The accumulation of propellant mass on the target may be indicated either by the slope of the balance output with the accelerating voltage on or by the total change in weight during a test divided by the time of the test (Figure 13).

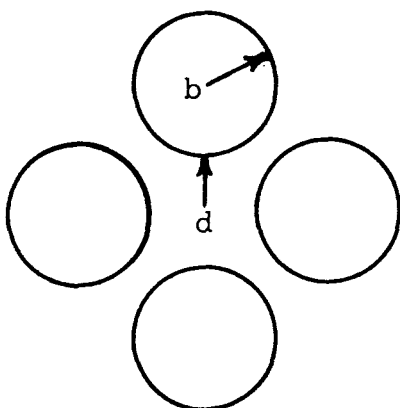
2.7 Massenfilter

A massenfilter has been built in order to supplement the information provided by the thrust, current, and mass flow measurements. This instrument not previously described in Reference 5, will be explained here in some detail. The quadrupole massenfilter was originally developed and built (References 8 and 9) as a precision instrument to separate isotopes, and its detailed theory has been given by its early developers. We shall summarize it here. The principle of the apparatus is that two particles of different charge-to-mass ratios will follow the same trajectory in a time-independent electric field (assuming no initial velocity), but will do so with different velocities. Thus, the two particles will follow different trajectories in a time-varying electric field. The time-dependent field chosen here is a quadratic field defined by the potential function:

$$U(x, y, z, t) = 1/2 (U_0 + U_1 \cos 2 \pi f t) \frac{(y^2 - x^2)}{d^2}$$

in an orthogonal system of coordinates. In this definition d is a constant, U_0 a constant potential, and U_1 the maximum amplitude of an alternating potential of frequency f . We shall show that such a field configuration can be obtained easily and that it is focusing along the z axis.

The field given above can be produced by imposing the appropriate potential values on two hyperbolic cylinders $y^2 - x^2 = \text{constant}$, for instance the value $\pm 1/2$



for instance the value $\pm 1/2$ $(U_0 + U_1 \cos 2 \pi f t)$ on the cylinder $y^2 - x^2 = \pm d^2$. To simplify the construction, one can replace the hyperbolae by tangent cylinders having a radius equal to their radius of curvature, i.e., d . This geometry would result in the desired field within a radius $2d/3$ (Ref. 9) around the z axis, but taking the radius of the cylinders $b = 1.16 d$ (Reference 10) gives an even better fit of the quadratic field.

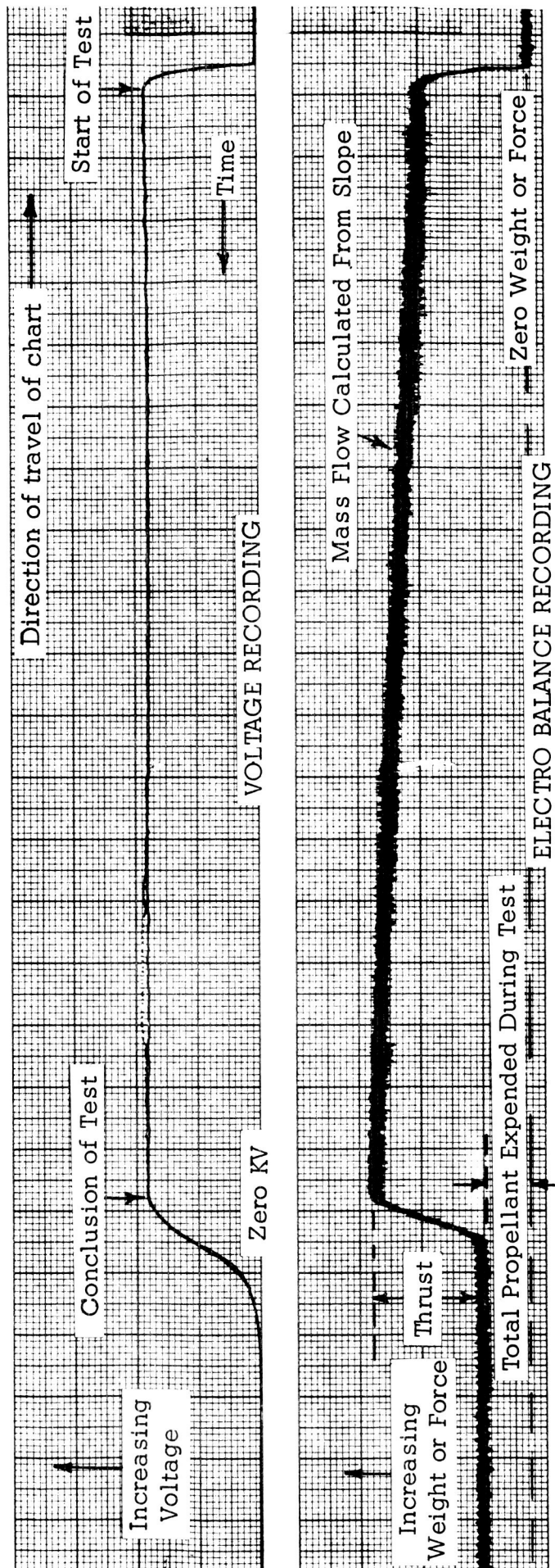


Figure 13. Typical Recordings of Voltage and Microbalance Output.

In the actual construction of the apparatus, cylinders of radius $b = 1.16d$ will be used, but in the following calculations hyperbolae $y^2 - x^2 = \pm d^2$ will be assumed. In these conditions the field is given by its coordinates:

$$E_x = - (U_0 + U_1 \cos 2 \pi f t) \frac{x}{d^2}$$

$$E_y = (U_0 + U_1 \cos 2 \pi f t) \frac{y}{d^2}$$

and the equations of motion are obtained by equating force to acceleration times mass:

$$\ddot{x} + (U_0 + U_1 \cos 2 \pi f t) \frac{x}{d^2} \frac{q}{m} = 0$$

$$\ddot{y} - (U_0 + U_1 \cos 2 \pi f t) \frac{y}{d^2} \frac{q}{m} = 0$$

$$\ddot{z} = 0.$$

For a particle of charge q/m which has been accelerated by a potential difference V the third equation gives

$$z = (2 \frac{q}{m} V)^{1/2} t.$$

With a new variable $T = \pi f t$ and with $G = \frac{U_1}{2 d^2} \frac{q}{m \pi^2 f^2}$, we have:

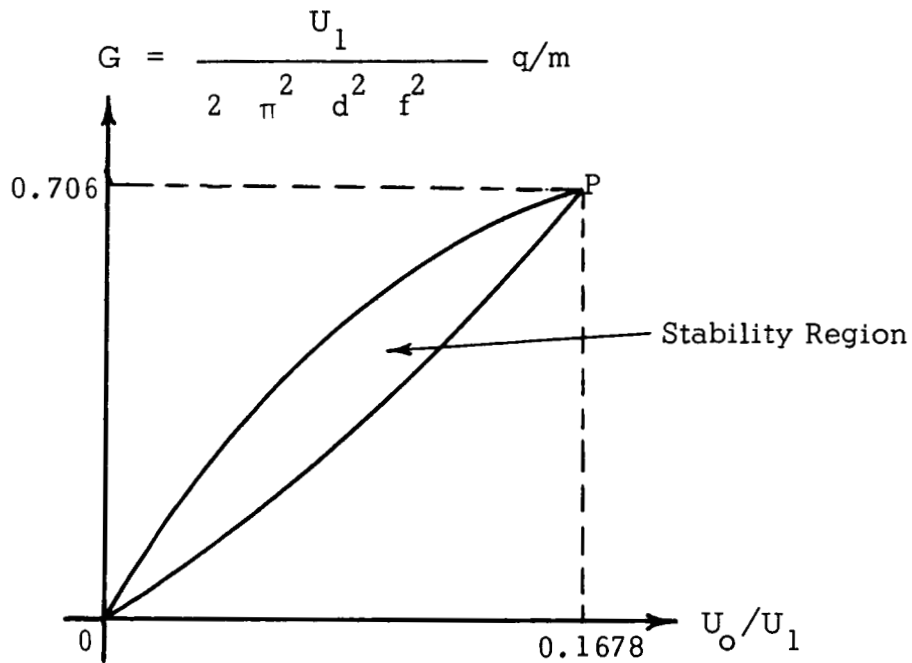
$$x + G (2 \frac{U_0}{U_1} + 2 \cos 2 T) x = 0$$

$$y - G (2 \frac{U_0}{U_1} + 2 \cos 2 T) y = 0.$$

This system is now written in the form of two Mathieu equations, each of which have two kinds of solutions: stable or unstable depending on the two parameters U_0/U_1 and G . If these parameters are chosen so that both equations have stable solutions, then the corresponding trajectories will be focused along the z axis. Nevertheless, stable trajectories may still be intercepted by the quadrupole if they result in an amplitude in the x, y plane greater than d . To determine the amplitude of the oscillations, one needs to introduce in addition the initial conditions: $x_0, y_0, \dot{x}_0, \dot{y}_0$. Conversely, if a trajectory is not stable the conditions may be such that a particle will not drift toward the rods of the quadrupole but will reach the target located at the other end of the device. It is easy enough to realize that a particle with initial conditions very close to $x_0 = y_0 = 0$ and $\dot{x}_0 = \dot{y}_0 = 0$ will not be affected by the field, even if the

equations of motion show an unstable trajectory. No satisfactory solution of this problem has been found to date. Discussions are found in the German literature which are directed toward low energy ions. No satisfactory discussion is found applicable to the range of charge- and energy-to-mass ratios represented by the colloids, and therefore, pending further analysis, the massenfilter should be used with caution as an instrument to evaluate charge-to-mass ratio distribution.

In the following we shall assume that the geometry of the massenfilter is such as to limit x_0 , y_0 and \dot{x}_0 , \dot{y}_0 sufficiently and that the particles stay in the massenfilter a sufficiently large number of cycles that the particle separation is determined by the stability and instability of the equations of motion. The conditions of stability as derived from the Mathieu equations (Reference 11) may be represented in a G , U_0/U_1 diagram as follows:



The presentation of this stability diagram is different from that used by Paul (References 8 and 9) but is utilized here as it shows separately the parameters usually kept constant during a test (U_0/U_1) and the variables U_1 or f . The diagram shows that for a value of $U_0/U_1 < 0.1678$ there will be a range of q/m such that stable solutions of the equations will be obtained and the corresponding particles will be collected by the target.

If it is desired that only a narrow band of q/m be accepted, then the value of U_0/U_1 will be chosen close to 0.1678 and the value of q/m may be close to that corresponding to point P, i.e., maximum resolution. In this case

$$q/m = 0.706 \frac{2 d^2 \pi^2 f^2}{U_1} = 13.93 \frac{d^2 f^2}{U_1}$$

The resolution may be calculated from the equations giving the upper and lower boundary of π . The calculations are tedious and we shall simply transcribe Paul's results for the parameter of interest q/m :

$$\frac{q/m}{\Delta q/m} = \frac{0.75}{1 - \frac{U_0}{U_1} 0.1678}.$$

The resolution therefore depends only on $\frac{U_0}{U_1}$ and not on d or f .

The above calculations have assumed an infinitely long quadrupole. In practice, the length L of the quadrupole will be determined by the number of times the particle will oscillate in the quadrupole. This is given by:

$$N = \frac{f L}{v} = f L (2 \frac{q}{m} V)^{-1/2}.$$

Introduction into the above equation of the value given earlier for q/m results in the elimination of f as follows:

$$N = 0.19 \frac{L}{d} \left(\frac{U_1}{V} \right)^{1/2}$$

Again, no satisfactory investigations have been made, and judging from the technical literature it seems that N should be greater than 25 or even 100. A rational choice is rendered difficult since previous investigators were concerned, as pointed out previously, with other types of particles and with acceleration voltage V lower than the quadrupole voltages U_0 and U_1 .

Finally, reasonable limits must be placed on the initial conditions. The entry window, which should be between $\frac{d}{2}$ and $\frac{d}{10}$ in radius according to the technical literature, will limit x_0 and y_0 . As to \dot{x}_0 and \dot{y}_0 , these should be very small with respect to v , for instance by two orders of magnitude. This last limitation can be estimated by comparing the focusing effect of a constant field of magnitude $U_0 + U_1$ applied approximately to the quadrupole with the defocusing effect of the initial slopes \dot{x}_0/v and \dot{y}_0/v . The limitation of \dot{x}_0 and \dot{y}_0 can be enforced by proper

orientation of the massenfilter to the beam. This is more difficult with the rotating nozzle than with a point source (needle).

Figure 14 shows the forward end of the quadrupole. The rails are made of precision ground 303 stainless steel rods. The housing is made of aluminum for lightness. A flexible 304 stainless steel bellows (Figure 10) is provided to permit orientation of the unit relative to the colloid beam. The input voltage is connected to the rails by means of a fabricated epoxy resin connector (Figure 15).

The circuit shown in Figure 16 was used to supply rail voltage. This circuit is capable of providing a voltage U_1 up to 2400 volts. As a first approximation the circuit was designed to provide continuous adjustment over a frequency range of 100 cycles to 100 kilocycles, covering the bandwidth of charge-to-mass ratios of greatest interest.

$$\text{The resolution given by } \frac{q/m}{\Delta q/m} = \frac{0.75}{1 - \frac{U_0}{0.1678 U_1}}$$

and $U_0 = \frac{1}{6} U_1$ is 111.

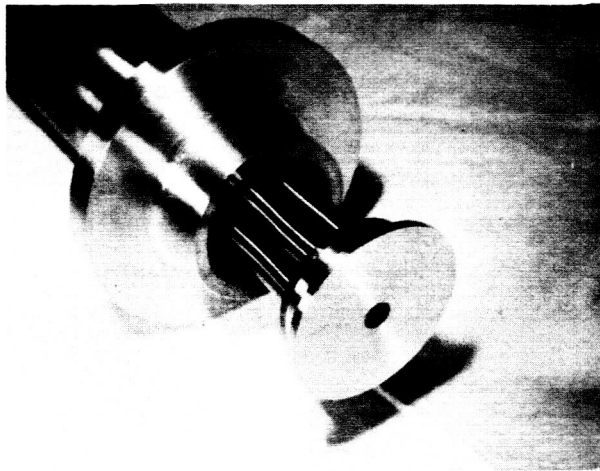


Figure 14. Massenfilter Quadrupole. Input end with rail assembly partially pulled out.

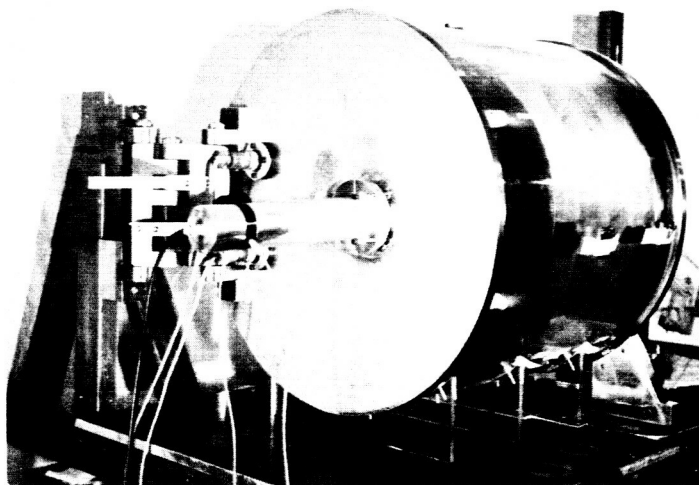
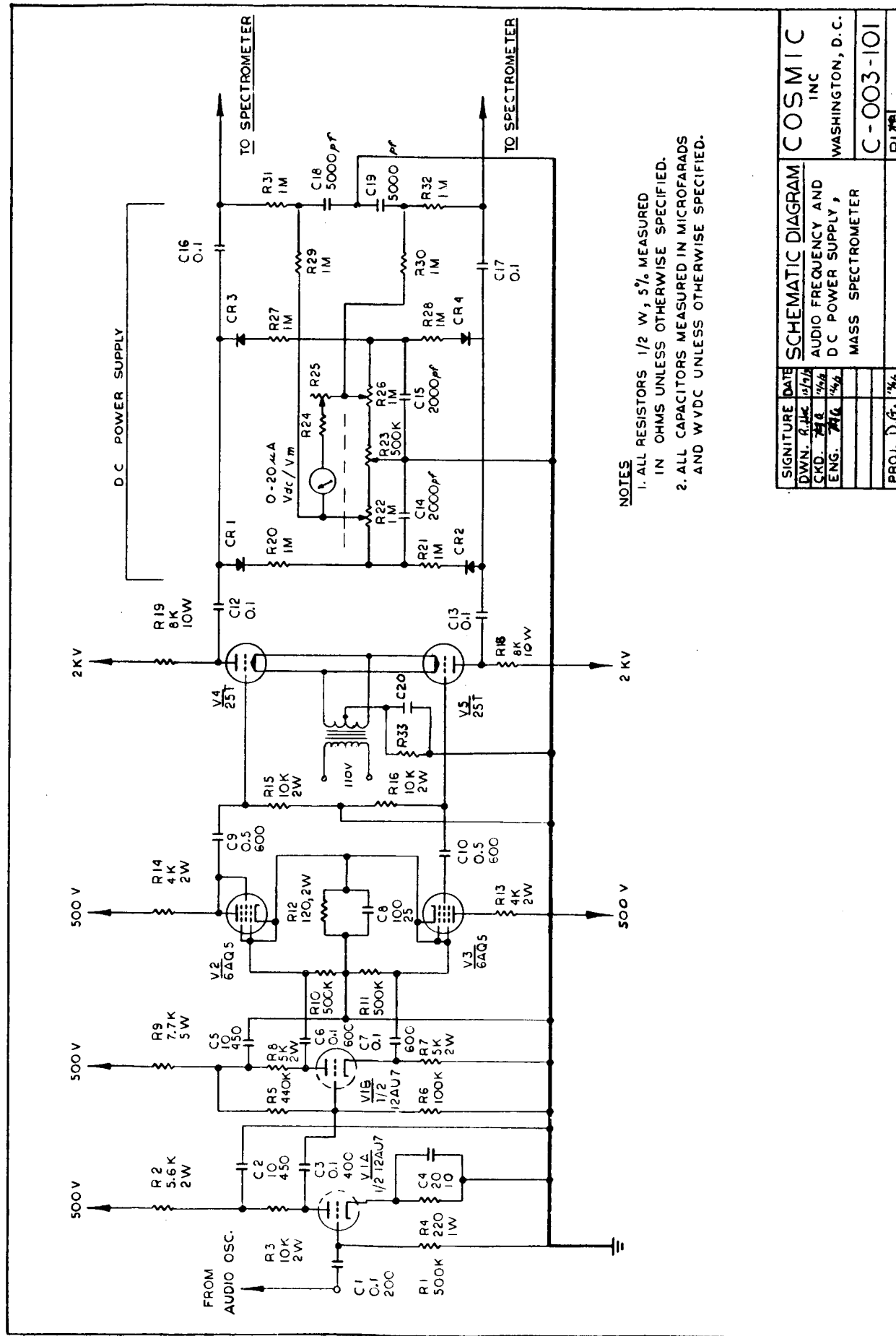


Figure 15. End Plate of Test Chamber with Adjustable Quadrupole.

Figure 16. Schematic Diagram. Audio Frequency and DC Power Supply, Mass Spectrometer



SIGNATURE	DATE	SCHEMATIC DIAGRAM	
DWN. R. J. C.	10/1/54	AUDIO FREQUENCY AND	COSMIC
CHKD. J. H. C.	10/1/54	DC POWER SUPPLY,	INC
ENG. J. H. C.	10/1/54	MASS SPECTROMETER	WASHINGTON, D. C.
PROJ. D. G.	10/1/54		C-003-101
			R1

3. THEORETICAL ANALYSIS OF SYSTEM PERFORMANCE

In the charged colloid source considered here, it is possible to vary independently the propellant, the nozzle and electrode geometries, the mass flow rate, \dot{m} , the nozzle's angular velocity, ω , and the accelerating voltage, V . In order to predict the influence of such variations upon system performance, a theoretical investigation was carried out and is summarized in this section. This investigation generalizes results previously obtained (Reference 5) and incorporates the effects of the propellant's surface tension, γ , capacitivity, ϵ , kinematic viscosity, ν , mass density, ρ_m , and conductivity, σ , as well as the effects of the size (characterized by the distance, L , between nozzle and extractor electrode) and shape (characterized by r/L , where r is the nozzle radius) of the nozzle-electrode configuration.

The system performance is characterized by the droplet charge-to-mass ratio, q/m , and the current, I , thrust, F , exhaust velocity, v , and power, P , of the beam of charged droplets. In any electrostatic thruster with particles of uniform charge-to-mass ratio, these quantities are related by

$$\begin{aligned} I &= \dot{m} (q/m) \\ F &= \dot{m} (2V)^{1/2} (q/m)^{1/2} \\ v &= (2V)^{1/2} (q/m)^{1/2} \\ P &= \dot{m} V (q/m) \end{aligned} \tag{1}$$

Thus, in order to predict system performance, it is sufficient to predict the variation of q/m with controllable elements. To this end, we shall now derive a suitable analytic representation for the charge-to-mass ratio.

Since the droplets are charged by induction, we have

$$\begin{aligned} q/m &= \frac{(\text{surface charge density}) (\text{droplet surface area})}{(\text{mass density}) (\text{droplet volume})} \\ &= \frac{K_1 Q}{\rho_m a} \end{aligned} \tag{2}$$

where

a = characteristic size of droplet

Q = surface charge density of droplet

K_1 = constant which depends on droplet shape (e.g.,
 $K_1 = 3$, for a spherical droplet)

In order for the droplet to remain intact, the cohesive stress ($\sim \gamma/a$) must exceed the disruptive stress ($\sim Q E_s$, where E_s is the electric field at the surface of the droplet) or, analytically,

$$a < \frac{K_3 \gamma}{Q E_s} \quad (3)$$

where the constant K_3 depends on droplet shape and is of order 1. (For a sphere, the conventional Rayleigh criterion corresponds to $K_3 = 4$, whereas, as shown in Reference 12, the value $K_3 = 1$ is suggested by considerations of minimum energy). In the charged colloid source considered here, the droplet size is comparable to the film thickness, h , provided the film is thin enough for Equation 3 to be satisfied; if the film is too thick, it disintegrates into smaller droplets for which Equation 3 is satisfied. Thus, we take

$$a = \begin{cases} K_2 h & K_2 h < K_3 \gamma / Q E_s \\ \frac{K_3 \gamma}{Q E_s} & K_2 h > K_3 \gamma / Q E_s \end{cases} \quad (4)$$

where K_2 is of order 1. Substitution of (4) into (2) gives

$$q/m = \begin{cases} \frac{K_1}{K_2} \frac{Q}{\rho_m h} & K_2 h < K_3 \gamma / Q E_s \\ \frac{K_1}{K_3} \frac{Q^2 E_s}{\rho_m \gamma} & K_2 h > K_3 \gamma / Q E_s \end{cases} \quad (5)$$

The surface charge density, Q , is influenced by the propellant conductivity, σ , and may be taken to be

$$Q = \epsilon E_s [1 - \exp(-\sigma \tau / \epsilon)] \quad (6)$$

where τ = characteristic time available for charging droplet

ϵ / σ = characteristic time for charging (cf. Ref. 13). Since Q depends upon the ill-understood hydrodynamics of the film instability, the actual situation is doubtless more complicated than Equation 6 suggests; nevertheless, this representation appears to be a reasonable approximation, provided τ is chosen properly. Substitution of (6) into (2), (4) and (5) gives

$$q/m = K_1 \frac{\epsilon E_s}{\rho_m a} [1 - \exp(-\sigma \tau / \epsilon)] \quad (7)$$

$$a = \begin{cases} K_2 h & K_2 h < \frac{K_3 \gamma}{\epsilon E_s^2 [1 - \exp(-\sigma \tau / \epsilon)]} \\ \frac{K_3 \gamma}{\epsilon E_s^2 [1 - \exp(-\sigma \tau / \epsilon)]} & K_2 h > \frac{K_3 \gamma}{\epsilon E_s^2 [1 - \exp(-\sigma \tau / \epsilon)]} \end{cases} \quad (8)$$

$$q/m = \begin{cases} \frac{K_1}{K_2} \frac{\epsilon E_s}{\rho_m h} [1 - \exp(-\sigma \tau / \epsilon)] & E_s^2 < \frac{K_3}{K_2} \frac{\gamma}{\epsilon h [1 - \exp(-\sigma \tau / \epsilon)]} \\ \frac{K_1}{K_3} \frac{\epsilon^2 E_s^3}{\rho_m \gamma} [1 - \exp(-\sigma \tau / \epsilon)]^2 & E_s^2 > \frac{K_3}{K_2} \frac{\gamma}{\epsilon h [1 - \exp(-\sigma \tau / \epsilon)]} \end{cases} \quad (9)$$

It is clear from Equation 9 that the droplet charge-to-mass ratio depends strongly upon the electric field, E_s . In the present application, $E_s = E_o$ where E_o is the field at the nozzle edge, where the droplet is formed. The field E_o serves both to charge and to accelerate the droplet and is influenced by space-charge effects, which we now discuss.

It is clear that for any space-charge flow, the electric field, E_o , at the source of charged particles decreases from the vacuum field, E_o^* , to zero as the current density, J , between the source and the accelerating electrode increases from zero to the space-charge-limited current density, J^* . Moreover, this variation can conveniently be described in terms of the normalized field, e_o , and the normalized current density, j , where

$$\begin{aligned} e_o &\equiv E_o/E_o^* \\ j &\equiv J/J^* \end{aligned} \quad (10)$$

Thus, for example, for a space-charge flow of particles with charge-to-mass ratio, q/m , passing between parallel plane electrodes separated by a distance, s , and a potential difference, V ,

$$E_o^* = V/s \quad (11)$$

$$J^* = \frac{4}{9} \frac{\epsilon_o (2 q/m)^{1/2} V^{3/2}}{s^2} \quad (12)$$

where ϵ_o = capacitivity of free space. Moreover, it is readily shown (cf. Ref. 5) that for this space-charge flow, e_o and j are related by

$$j = \frac{1}{2} \left[1 \pm \left\{ 1 - \frac{27}{4} e_o^2 (1 - e_o) \right\}^{1/2} \right] \quad \begin{aligned} 0 \leq e_o \leq 2/3 \\ 2/3 \leq e_o \leq 1 \end{aligned} \quad (13)$$

The significant points here are that, for any space-charge flow, i) the normalizing field, E_o^* , and current density, J^* , must, by dimensional analysis, have the form

$$E_o^* = V/l \quad (14)$$

$$J^* = B \epsilon_o (q/m)^{1/2} V^{3/2} / l^2 \quad (15)$$

where l is a characteristic length of the electrode system (e.g., the electrode separation, for the parallel-plane geometry) and B is a dimensionless parameter dependent upon electrode geometry (e.g., $B = 4\sqrt{2}/9$ for the parallel-plane geometry), ii) it is possible to establish a relation between e_o and j and iii) this relation satisfies

$$e_o (j = 0) = 1$$

$$e_o (j = 1) = 0$$

In particular, for the colloidal generating system considered here, such a relation exists and weak space-charge effects correspond to small currents, i.e., $j \ll 1$, and large space-charge effects correspond to large currents, i.e., $e_o \ll 1$.

For any geometry, solution of the purely electrostatic problem ($J = 0$) provides E_o^* and thus $l \equiv V/E_o^*$, while solution of the space-charge limit problem ($E_o = 0$) provides J^* and thus $B \equiv J^* l^2 / \epsilon_o (q/m)^{1/2} V^{3/2}$.

Solution of the intermediate problem provides functions H and K such that

$$\begin{aligned} e_o &= K(j) \\ j &= H(e_o) \end{aligned} \tag{16}$$

Thus H and K are mutually inverse, monotonically decreasing functions from $(0, 1)$ to $(0, 1)$. For the parallel plane geometry, Equations 11 and 12 give $l = s$ and $B = 4\sqrt{2/9}$, respectively, while Equation 13 gives H, which is shown in Figure 17, along with its inverse, K.

In deriving an analytic representation of the charge-to-mass ratio, we shall encounter equations of the form

$$j = (e_o \alpha)^{n/2}$$

where α is a dimensionless parameter which depends upon controllable elements and n is a positive exponent which expresses the power-law dependence of charge-to-mass ratio upon electric field (i.e., $q/m \sim E_s^n$). An equation of this form may be written as

$$\alpha = e_o^{-1} j^{2/n}$$

or, by (16),

$$\alpha = e_o^{-1} H^{2/n}(e_o)$$

In a more compact notation, we write

$$\alpha = f_n(e_o)$$

where the functions f_n , $n > 0$, are defined mathematically by

$$f_n(x) = x^{-1} H^{2/n}(x) \quad 0 < x < 1 \tag{17}$$

for any positive real number n , and any real argument x in $(0, 1)$. We note that, for all n , f_n is a smooth monotonically decreasing function from $(0, 1)$ to $(0, \infty)$ with $f_n(0) = \infty$, $f_n(1) = 0$. Consequently, it is meaningful to invert the next-to-last equation to obtain

$$e_o = g_n(\alpha)$$

where the inverse functions g_n , $n > 0$, are defined mathematically by

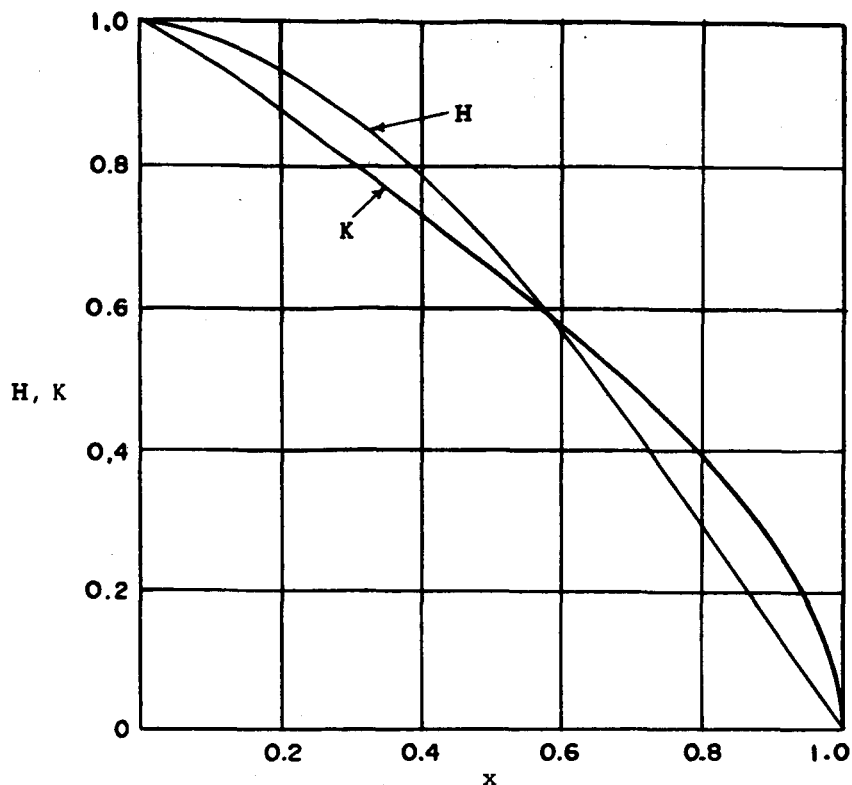


Figure 17. The Functions $j = H(e_o)$ and $e_o = K(j)$, Relating Dimensionless Source Field, e_o , and Dimensionless Current Density, j , for Space Charge Flow Between Parallel Planes

$$g_n(x) = f_n^{-1}(x) \quad 0 < x < \infty \quad (18)$$

for any positive real number n , and any real argument x . We note that, for all n , g_n is a monotonically decreasing function from $(0, \infty)$ to $(0, 1)$ with $g_n(0) = 1$, $g_n(\infty) = 0$. Moreover, we have, for $n > 0$,

$$f_n(x) \approx x^{-1} \quad x \ll 1 \quad (19)$$

$$g_n(x) \approx \begin{cases} 1 & x \ll 1 \\ x^{-1} & x \gg 1 \end{cases} \quad (20)$$

Figure 18 shows the function $g_1(x)$ for the parallel plane geometry. It must be emphasized that the parameters l and B and the functions H , K , f_n , g_n depend upon geometry (cf. Ref. 14), e.g., upon the ratio of inner to outer radii for concentric spheres or coaxial cylinders and upon parameters such as r/L in the charged colloid source considered here.

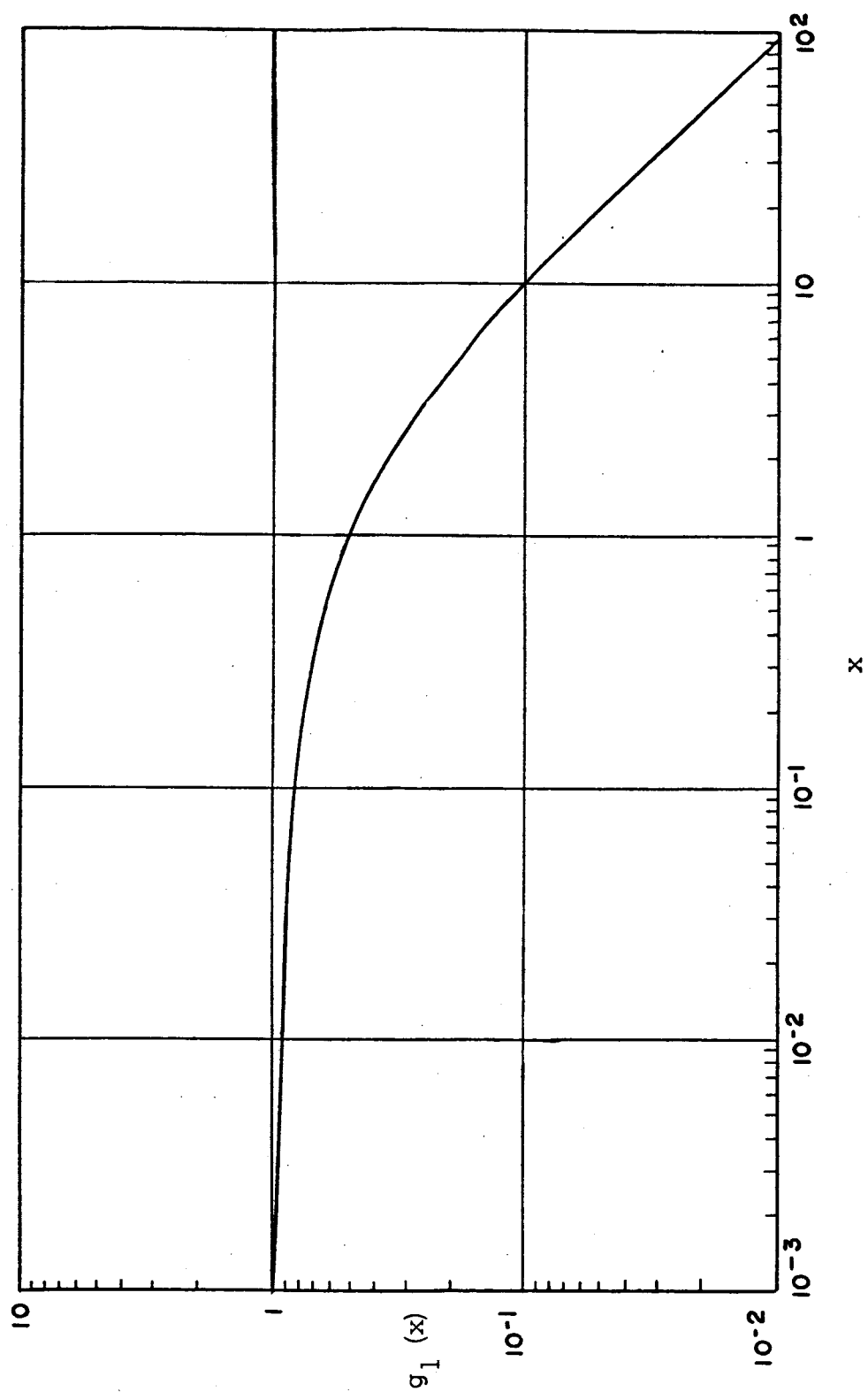


Figure 18. The Function $g_1(x)$ Defined by Space-Charge Flow Between Parallel Planes.

For the geometry considered in the present application, no solution of the purely electrostatic problem, let alone the space-charge problem, exists. Hence, we introduce a parameter K_4 , defined by

$$K_4 = \frac{E_o^*}{V/L} \quad (21)$$

where, it will be recalled, L is the distance between the nozzle and the extractor electrode. The sharpness of the nozzle's edge guarantees that $K_4 \gg 1$. By (14), (21) is equivalent to

$$1 = \frac{L}{K_4} \ll L \quad (22)$$

Combination of (10) and (21) gives

$$E_o = \frac{K_4 V}{L} e_o \quad (23)$$

Substitution of (23) into (9) gives

$$q/m = \begin{cases} (q/m)_1 e_o & e_o \leq \Gamma \\ (q/m)_3 e_o^3 & e_o \geq \Gamma \end{cases} \quad (24)$$

where

$$(q/m)_1 \equiv \frac{C_1 \epsilon V}{\rho_m L h} [1 - \exp(-\sigma \tau / \epsilon)] \quad (25)$$

$$(q/m)_3 \equiv \frac{C_3^3 \epsilon^2 V^3}{\rho_m \gamma L^3} [1 - \exp(-\sigma \tau / \epsilon)]^2 \quad (26)$$

$$C_1 \equiv K_1 K_4 / K_2 \quad (27)$$

$$C_3^3 \equiv K_1 K_4^3 / K_3 \quad (28)$$

$$\Gamma \equiv \frac{L}{V} \left(\frac{C_1}{C_3^3} \frac{\gamma}{\epsilon h} \right)^{1/2} [1 - \exp(-\sigma \tau / \epsilon)]^{-1/2} \quad (29)$$

Since K_1 , K_2 , and K_3 are of order 1, it follows that $C_1 \approx C_3 \approx K_4 \gg 1$.

The desired analytic representation of the droplet charge-to-mass ratio now follows directly. From (1), the current density, J , of the beam is

$$J = (\dot{m}/A) (q/m) \quad (30)$$

where A = emissive area

Moreover, from (15) and (22),

$$J^* = B K_4^2 \epsilon_0 (q/m)^{1/2} V^{3/2} / L^2 \quad (31)$$

Equations 10, 30 and 31 then give

$$j = \frac{J}{J^*} = (q/m)^{1/2} \frac{(\dot{m}/A) L^2}{B K_4^2 \epsilon V^{3/2}} \quad (32)$$

Therefore, by (24)

$$j = \begin{cases} (e_0 \lambda)^{1/2} & e_0 \leq \Gamma \\ (e_0 \mu)^{3/2} & e_0 \geq \Gamma \end{cases} \quad (33)$$

where

$$\lambda \equiv \frac{(\hat{q}/m)_1 (\dot{m}/A)^2 L^4}{(B K_4^2)^2 \epsilon^2 V^3} \quad (34)$$

$$\mu \equiv \lambda^{1/3} / \Gamma^{2/3} = \frac{(\hat{q}/m)_3^{1/3} (\dot{m}/A)^{2/3} L^{4/3}}{(B K_4^2)^{2/3} \epsilon^{2/3} V} \quad (35)$$

It follows from (16) and (17) that

$$\begin{aligned} \lambda &= f_1(e_0) & e_0 &\leq \Gamma \\ \mu &= f_3(e_0) & e_0 &\geq \Gamma \end{aligned} \quad (36)$$

These relations may be inverted, by (18), to give

$$e_0 = \begin{cases} g_1(\lambda) & \lambda > \lambda^* \equiv f_1(\Gamma) \\ g_3(\mu) & \mu < \mu^* \equiv f_3(\Gamma) \end{cases} \quad (37)$$

or alternatively,

$$e_o = \begin{cases} g_1(\lambda) & \lambda > \lambda^* \equiv f_1(\Gamma) \\ g_3(\lambda^{1/3}/\Gamma^{2/3}) & \lambda < \lambda^* \equiv f_1(\Gamma) \end{cases} \quad (38)$$

In these and subsequent expressions, $f_1(\Gamma)$ and $f_3(\Gamma)$ are defined to be zero, for $\Gamma > 1$.

Substitution of (38) into (24) gives

$$q/m = \begin{cases} (\hat{q}/m)_1 g_1(\lambda) & \lambda > \lambda^* \equiv f_1(\Gamma) \\ (\hat{q}/m)_3 [g_3(\lambda^{1/3}/\Gamma^{2/3})]^3 & \lambda < \lambda^* \equiv f_1(\Gamma) \end{cases} \quad (39)$$

We recall that the film thickness, h , is given (Ref. 6) by

$$h = \left(\frac{\nu \dot{m}}{D \rho_m r^2 \omega^2} \right)^{1/3} \quad (40)$$

where D is of order 1. (For a conical nozzle of semi-vertex angle α , $D = (2 \pi/3) \sin \alpha$). The emissive area is

$$A = 2 \pi r h \quad (41)$$

Substitution of (40) and (41) into (25), (26), (29), (34), and (35) gives

$$(\hat{q}/m)_1 = C_1 D^{1/3} \frac{\epsilon V}{L^{1/3}} \dot{m}^{-1/3} \omega^{2/3} (r/L)^{2/3} (\rho_m \nu)^{-1/3} [1 - \exp(-\sigma \tau / \epsilon)] \quad (42)$$

$$(\hat{q}/m)_3 = C_3^3 \frac{\epsilon^2 V^3}{L^3} (\rho_m \nu)^{-1} [1 - \exp(-\sigma \tau / \epsilon)]^2 \quad (43)$$

$$\lambda = \frac{C_1 D}{(2 \pi B K_4)^2} \frac{L^3}{\epsilon V^2} \dot{m} \omega^2 \nu^{-1} [1 - \exp(-\sigma \tau / \epsilon)] \quad (44)$$

$$\Gamma = \left(\frac{C_1 D^{1/3}}{C_3} \right)^{1/2} \frac{L^{4/3}}{\epsilon^{1/2} V} \dot{m}^{-1/6} \omega^{1/3} (r/L)^{1/3} \left(\frac{\nu^3 \rho_m}{V} \right)^{1/6} \quad (45)$$

$$[1 - \exp(-\sigma \tau / \epsilon)]^{-1/2}$$

$$\mu = \frac{C_3 D^{2/9}}{(2 \pi B K_4)^{2/3}} L^{1/9} m^{4/9} \omega^{4/9} (r/L)^{-2/9} (\gamma^3 \rho_m v^2)^{-1/9} [1 - \exp(-\sigma \tau / \epsilon)]^{2/3} \quad (46)$$

Thus, Equation 39, supplemented by Equations 42 through 46, is the desired analytic representation of the droplet charge-to-mass as a function of controllable elements.

The derivation presented above reflects the fact that droplets may be formed by either of two modes, viz., i) extraction, wherein droplets have a characteristic size of roughly the film thickness at the edge of the nozzle, and ii) disintegration, wherein, because the film is relatively thick, droplets have a characteristic size dictated by a Rayleigh-like stability criterion. From Equation 39, the extraction (E) and disintegration (D) modes correspond to λ greater and less than $f_1(\Gamma)$, respectively. (It should be noted that the results presented in Ref. 5 correspond precisely to those presented above for the extraction mode; the parameter " λ " introduced above was designated " Ω " in Ref. 5). Before discussing more general performance trends predicted by Equation 39, it is profitable to consider the limiting cases corresponding to strong and weak space-charge effects, respectively.

It is clear, from (20) and (37), that in the strong space-charge limit ($e_0 \ll 1$),

$$e_0 \approx \begin{cases} \lambda^{-1} & \text{E mode, } \lambda \gg 1 \\ \mu^{-1} = \Gamma^{2/3} \lambda^{-1/3} & \text{D mode, } \mu \gg 1 \end{cases} \quad (47)$$

Substitution of (47) into (39) gives

$$(q/m) \approx \begin{cases} (\hat{q}/m)_1 \lambda^{-1} & \text{E mode} \\ (\hat{q}/m)_3 \mu^{-3} & \text{D mode} \end{cases} \quad (48)$$

Substitution of (42), (43), (44), (46) into (48) shows that in both the D and E modes, the charge-to-mass ratio in the strong space-charge limit assumes a common value, $(q/m)^*$, given by

$$q/m = (q/m)^* = (2 \pi B K_4)^{2/3} D^{-2/3} \frac{\epsilon^2 v^3}{L^{10/3}} m^{-4/3} \omega^{-4/3} (r/L)^{2/3} \left(\frac{v}{\rho_m}\right)^{2/3} \quad (49)$$

Substitution of (49) into (1) furnishes the other performance characteristics in the strong space-charge limit as

$$I = I^* \equiv \dot{m} (q/m)^* \\ = (2 \pi B K_4^2)^2 D^{-2/3} \frac{\epsilon^2 V^3}{L^{10/3}} \dot{m}^{-1/3} \omega^{-4/3} (r/L)^{2/3} \left(\frac{v}{\rho_m} \right)^{2/3} \quad (50)$$

$$F = F^* \equiv \dot{m} (2 V)^{1/2} (q/m)^*^{1/2} \\ = (2 \pi B K_4^2)^2 2^{1/2} D^{-1/3} \frac{\epsilon^{1/2} V^2}{L^{5/3}} \dot{m}^{1/3} \omega^{-2/3} (r/L)^{1/3} \left(\frac{v}{\rho_m} \right)^{1/3} \quad (51)$$

$$v = v^* \equiv (2 V)^{1/2} (q/m)^*^{1/2} \\ = (2 \pi B K_4^2)^2 2^{1/2} D^{-1/3} \frac{\epsilon^{1/2} V^2}{L^{5/3}} \dot{m}^{-2/3} \omega^{-2/3} (r/L)^{1/3} \left(\frac{v}{\rho_m} \right)^{1/3} \quad (52)$$

$$P = P^* \equiv \dot{m} V (q/m)^* \\ = (2 \pi B K_4^2)^2 D^{-2/3} \frac{\epsilon V^4}{L^{10/3}} \dot{m}^{-1/3} \omega^{-4/3} (r/L)^{2/3} \left(\frac{v}{\rho_m} \right)^{2/3} \quad (53)$$

In the weak space-charge limit, the performance is different in the two modes. In the extraction mode (corresponding, by (20), to sufficiently small λ), combination of (1), (39) and (42) gives

$$q/m = (\hat{q}/m)_1 \\ = C_1 D^{1/3} \frac{\epsilon_0 V}{L^{1/3}} \dot{m}^{-1/3} \omega^{2/3} (r/L)^{2/3} (\rho_m^2 v)^{-1/3} [1 - \exp(-\sigma \tau / \epsilon)] \quad (42)$$

$$I = \hat{I}_1 \equiv \dot{m} (\hat{q}/m)_1 \\ = C_1 D^{1/3} \frac{\epsilon_0 V}{L^{1/3}} \dot{m}^{2/3} \omega^{2/3} (r/L)^{2/3} (\rho_m^2 v)^{-1/3} [1 - \exp(-\sigma \tau / \epsilon)] \quad (54)$$

$$\begin{aligned}
F &= \hat{F}_1 \equiv \dot{m} (2V)^{1/2} (\hat{q}/m)_1^{1/2} \\
&= (2C_1)^{1/2} D^{1/6} \frac{\epsilon_o^{1/2} V}{L^{1/6}} \dot{m}^{5/6} \omega^{1/3} (r/L)^{1/3} (\rho_m^2 \nu)^{-1/6} [1 - \exp(-\sigma\tau/\epsilon)]^{1/2}
\end{aligned} \tag{55}$$

$$\begin{aligned}
v &= \hat{v}_1 \equiv (2V)^{1/2} (\hat{q}/m)_1^{1/2} \\
&= (2C_1)^{1/2} D^{1/6} \frac{\epsilon_o^{1/2} V}{L^{1/6}} \dot{m}^{-1/6} \omega^{1/3} (r/L)^{1/3} (\rho_m^2 \nu)^{-1/6} [1 - \exp(-\sigma\tau/\epsilon)]
\end{aligned} \tag{56}$$

$$\begin{aligned}
P &= \hat{P}_1 \equiv \dot{m} V (\hat{q}/m)_1 \\
&= C_1 D^{1/3} \frac{\epsilon_o V^2}{L^{1/3}} \dot{m}^{2/3} \omega^{2/3} (r/L)^{2/3} (\rho_m^2 \nu)^{-1/3} [1 - \exp(-\sigma\tau/\epsilon)]
\end{aligned} \tag{57}$$

In the disintegration mode (corresponding by (20) to sufficiently small μ) combination of (1), (39), and (43) gives, in the weak space-charge limit,

$$q/m = (\hat{q}/m)_3 = C_3^3 \frac{\epsilon_o^2 V^3}{L^3} (\rho_m \gamma)^{-1} [1 - \exp(-\sigma\tau/\epsilon)]^2 \tag{43}$$

$$I = \hat{I}_3 \equiv \dot{m} (\hat{q}/m)_3 = C_3^3 \frac{\epsilon_o^2 V^3}{L^3} \dot{m} (\rho_m \gamma)^{-1} [1 - \exp(-\sigma\tau/\epsilon)]^2 \tag{58}$$

$$\begin{aligned}
F &= \hat{F}_3 \equiv \dot{m} (2V)^{1/2} (\hat{q}/m)_3^{1/2} \\
&= 2^{1/2} C_3^{3/2} \frac{\epsilon_o V^2}{L^{3/2}} \dot{m} (\rho_m \gamma)^{-1/2} [1 - \exp(-\sigma\tau/\epsilon)]
\end{aligned} \tag{59}$$

$$\begin{aligned}
v &= \hat{v}_3 \equiv (2V)^{1/2} (\hat{q}/m)_3^{1/2} \\
&= 2^{1/2} C_3^{3/2} \frac{\epsilon_o V^2}{L^{3/2}} (\rho_m \gamma)^{-1/2} [1 - \exp(-\sigma\tau/\epsilon)]^{1/2}
\end{aligned} \tag{60}$$

$$P = \hat{P}_3 \equiv \dot{m} V (\hat{q}/m)_3 = C_3^3 \frac{\epsilon_0^2 V^4}{L^3} \dot{m} (\rho_m \gamma)^{-1} [1 - \exp(-\sigma \tau / \epsilon)]^2 \quad (61)$$

The results derived above demonstrate that the space-charge behavior of the system is dictated by two dimensionless parameters λ and μ or, equivalently, λ and Γ . (An analogous result in fluid mechanics states that the behavior of a wide class of flows is dictated by the Mach number and Reynolds number.) The effects of varying controllable elements may conveniently and instructively be represented geometrically in the $\lambda - \Gamma$ plane. However, we shall here defer such geometric interpretations and consider the influence of \dot{m} , ω , V and propellant properties ρ_m , γ , ν , and σ upon charge-to-mass ratio. Analogous results are readily derived for beam current, thrust, exhaust velocity and power. We do not consider variations in (r/L) since the solution (and thus B , f_1 , g_1 , g_3 , etc.) of the space-charge problem depends upon (r/L) . Likewise, we do not consider variations in L , since variation in size alone is operationally uninteresting. In this discussion, we ignore the characteristic time, τ ; more accurately, we ignore the implicit dependence of τ upon \dot{m} , ω , and propellant.

We consider first the influence of voltage upon charge-to-mass ratio. Since $\Gamma \sim V^{-1}$ and f_1 is a decreasing function, $f_1(\Gamma)$ vanishes for sufficiently small V and then increases steadily. Conversely $\lambda \sim V^{-2}$, and λ decreases steadily for increasing V . Consequently, the system operates in the E mode ($\lambda > f_1(\Gamma)$), for sufficiently small V and in the D mode for larger V . In the E mode, $(\hat{q}/m)_1 \sim V$ while e_o also increases with increasing V , since $\lambda \sim V^{-2}$. Thus $q/m_1 = (\hat{q}/m)_1 e_o$ is an increasing function of V in the E mode. In the D mode, $(\hat{q}/m)_3 \sim V^3$ and e_o is independent of V since μ is independent of V . Thus $q/m = (\hat{q}/m)_3 e_o^3$ is an increasing ($\sim V^3$) function of V in the D mode also. In summary, the charge-to-mass ratio is an increasing function of V , for all V . The transition, if any, to strong space-charge effects is determined by the values of the other parameters being held constant while V is varied.

Completely analogous considerations shows that as \dot{m} alone is varied, the system operates in the E mode for sufficiently small and large \dot{m} , and in the D mode for some intermediate range of \dot{m} , if at all. Likewise q/m is a steadily decreasing function of \dot{m} , for all \dot{m} , in both the E and D modes. Similarly, as ω alone is varied, the system operates in the D mode for sufficiently small ω and in the E mode for all larger ω . In the D mode, q/m is a decreasing function of ω . In the E mode, q/m may possibly increase with ω in some intermediate ranges but ultimately decreases with ω for all sufficiently large ω . Strong space-charge effects necessarily occur for sufficiently large \dot{m} or ω .

The effects of varying a single propellant property are determined similarly. The system operates in the D and E modes for sufficiently small and large ρ_m , respectively. Charge-to-mass ratio is a steadily decreasing function of ρ_m , for all ρ_m . The transition, if any, to strong space-charge effects, is determined by the other parameters. The influence of γ upon q/m is the same as that of ρ_m , except that q/m approaches a finite limit, rather than zero, for sufficiently large γ . The system operates in the E and D modes for sufficiently small and large ν , respectively. In the E mode, q/m is an increasing function of ν for sufficiently small ν but may be decreasing for some range of larger ν . In the D mode, q/m is a steadily increasing function of ν . Strong space-charge effects necessarily occur for sufficiently small ν . Finally, the system operates in the E mode for at least sufficiently small σ and in the D mode, if at all, only for all larger values of σ . In both the E and D modes, q/m is a steadily increasing function of σ , and approaches a finite limit for sufficiently large σ . The transition, if any, to strong space-charge effects is determined by the other parameters held constant while σ is varied.

4. CHEMICAL INVESTIGATIONS

The predicted influence of propellant upon system performance has been couched in terms of such macroscopic properties as density, surface tension, viscosity, and conductivity. By means of the theory presented in the preceding section, it is possible to prescribe desirable combinations of such properties. In order to qualify as a propellant, a substance must also meet compatibility requirements such as stability, a sufficiently low vapor pressure, and the ability to wet metal surfaces. Since all these requirements are described macroscopically, rather than structurally, the search for a satisfactory propellant remains essentially empirical and must be guided by fundamental principles of chemical structure. To this end, a chemical investigation was carried out, aimed at systematically varying the composition of certain organic solutions and evaluating their potential as propellants. The results of this investigation are summarized in this section.

The requirement of low vapor pressure ($< 10^{-6}$ mm/Hg) is satisfied by numerous organic solvents. The further restrictions of low resistivity and high stability severely limit the number of solvents which may be used. Under the general term stability we include:

- (a) absence of chemical reaction between solvent and solute
- (b) stability upon storage
- (c) stability towards charging
- (d) absence of tendency towards chemical disproportionation, polymerization or oxidative decomposition.

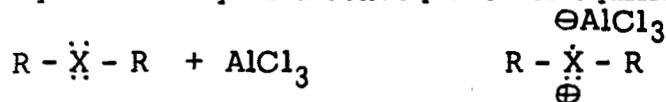
Since vapor pressure is related to intermolecular association and molecular weight, the solvents of choice are those with molecular weight in the range of 300 to 1500. Polymolecular association results from hydrogen bonding, the strength of which may range from 2 to 20 kcal/mole. Therefore, polyhydroxy solvents are of particular interest. Generally polar solvents will be associated intramolecularly due to short range electrostatic attraction, dispersion forces and miscellaneous non-saturative complexation phenomena. The ability of a solvent to dissolve an organic solute requires (among other things) the presence of polar groups within the solvent. Thus, solvents containing ester, oxide, carbonyl, silyl and ether functional groups have proven useful.

In order to decrease the resistivity of suitable solvents, a number of solutes were investigated. The effect of solute upon resistivity of the pure solvent is presented in Table II. The main classes of solutes used were:

- (a) ionic salts which would be partially dissociated in solution
- (b) covalent salts which might polarize the solvent molecules
- (c) organic and inorganic acids
- (d) Lewis acids
- (e) organic and inorganic bases
- (f) compounds with large quenching cross-sections for electrons.

Consistent decreases in the resistivity of octoil and dibutyl phthalate were obtained by addition of tetra-n-butyl ammonium picrate (TNBAP) to the pure solvent. Since the resistivity was observed to be a decreasing function of the percentage of TNBAP and the limiting factor in this system was the solubility of TNBAP in the solvent, we examined other quaternary ammonium salts related to TNBAP. Although Triton A (benzyltrimethyl ammonium methoxide) and Triton B (benzyltrimethyl ammonium hydroxide) gave solutions in octoil which had very low resistivity, the instability of these materials eliminated them as useful solutes. Furthermore, Triton B proved to be too highly hygroscopic. Undoubtedly, other quaternary picrates, benzoates or phenols might give more highly conducting solutions and yet not possess the undesirable properties of Triton B and tetra-methylammonium hydroxide. Investigation of such materials is contemplated.

Reference to Table III reveals that the Lewis acid aluminum chloride in combination with oxygenated solvents yields solutions of diminished resistivity. This may be a consequence of equilibria involving:



in which X = carbonyl, ester, nitrile, ether, amine. Such charge aggregates would increase the conductivity of the solution. Reduced resistivity with zinc chloride, antimony trichloride and aluminum bromide may be ascribed to a similar effect. Boron trifluoride should also be used and will be in a future study.

TABLE II. Summary of Resistivity Tests

SOLVENT	SOLUTE	RESISTIVITY Ohms-cm	REMARKS
Octoil (2-Ethyl hexyl phthalate)	None	4×10^9	
	Lithium Iodide	5×10^5	
	Triton A 10%	5×10^4	
	Triton B 10%	1.5×10^5	
	1-Naphthol-Sulfonic Acid	1.5×10^6	
	Diocetyl Sodium Sulfosuccinate	4×10^6	
Dibutyl phthalate	Tetra-N-butyl ammonium picrate (TNBAP)	1×10^6	
	None	5×10^9	
	Tetra-N-butyl ammonium picrate (TNBAP)	5×10^4	
	Lithium Iodide	1.5×10^6	
	Lanthanum Chloride	1.5×10^8	
	Triton + TNBAP	1.3×10^5	
Glycerin	Antimony Trichloride	6×10^4	
	Antimony Trichloride + TNBAP	1.5×10^4	
	Sulfuric Acid	9×10^4	
	None	$2.4-5 \times 10^6$	
	Antimony Trichloride	2×10^3	
	Cab-O-Sil	4×10^5	
Di Isooctyl Phthalate	Lithium Iodide	2.5×10^3	
	Lithium Bromide	2.5×10^4	
Di Tridecyl Phthalate	None	$> 10^{10}$	
	Lithium Iodide	8.5×10^7	
Di Isodecyl Phthalate	None	$\sim 2 \times 10^9$	
	Lithium Iodide	1×10^5	
Di Isodecyl Phthalate	None	> 10	
	Lithium Iodide	1.5×10^6	

TABLE II. (continued)

SOLVENT	SOLUTE	RESISTIVITY Ohms-cm	REMARKS
Tricresylphosphate	Lithium Iodide Tetra-N-Butyl ammonium picrate (TNBAP) Antimony Trichloride Sulfuric Acid	6×10^4 3×10^5 2.2×10^6 1×10^6	
PG 1200 (Monsanto)	None Lithium Iodide Lithium Bromide Tetra-N-Butyl ammonium picrate (TNBAP) Antimony Trichloride Bismuth Chloride	3×10^8 5.6×10^4 2.5×10^5 4×10^6 8×10^5 3×10^8	
Carbowax 550	None Lithium Bromide Tetra-N-Butyl ammonium picrate (TNBAP) 4% Ferrous Iodide Cab-O-Sil N, N Diphenylformamide Polyphosphoric Acid	8.2×10^5 1×10^4 1.4×10^5 4.5×10^4 1.7×10^5 4×10^6 1×10^4	
Niax (Union Carbide)	Tetra-N-Butyl ammonium picrate (TNBAP) Lithium Bromide	8×10^7 4×10^5	very low solubility
Pluracol P 410 (Wyandotte Chemical Corp)	None Tetra-N-Butyl ammonium picrate (TNBAP) Lithium Bromide N, N Diphenylformamide Carbowax 20 M	9×10^6 2×10^5 4.5×10^4 1.3×10^7 $> 10^{10}$	saturates < 4% dissolves with heat but re- crystallizes
Pluracol P 1010 (Wyandotte Chemical Corp)	None Tetra-N-Butyl ammonium picrate (TNBAP) Lithium Bromide	$> 10^{10}$ 1.3×10^7 1.9×10^5	poor solubility

TABLE II. (continued)

SOLVENT	SOLUTE	RESISTIVITY Ohms-cm	REMARKS
Sirbitol	None	10^4	
	Tetra-N-Butyl ammonium picrate (TNBAP)	8×10^3	
	Antimony Trichloride	4.8×10^2	
	Bismuth Chloride	4×10^3	
OS-124 (Monsanto)	Tetra-N-Butyl ammonium picrate (TNBAP)	2×10^7	poor solubility
	Antimony Trichloride	4.5×10^8	
	Sulfuric Acid	$> 10^9$	
	Lithium Iodide	$> 10^{10}$	
Aroclor 1248 (Monsanto)	Tetra-N-Butyl ammonium picrate (TNBAP)	3×10^3	poor solubility
	Antimony Trichloride Lithium Iodide	1.5×10^5 $> 10^{10}$	
Aroclor 1254 (Monsanto)	Antimony Trichloride	1.5×10^5	poor solubility
HB-40	Antimony Trichloride	$> 10^{10}$	poor solubility
	Carbowax 20 M	$> 10^{10}$	
Dow-200 Silicone Oil	Antimony Trichloride	$> 10^{10}$	insoluble
	Lithium Iodide	$> 10^{10}$	
None PG1200 Octoil Carbowax 550	Diocylsodium sulfosuccinate in 75% stabilizer (DSS)	1×10^4	vapor pressure too high " "
	"	4×10^4	
	"	4×10^6	
	DSS without stabilizer + Lithium Bromide	2.2×10^4	

TABLE II. (continued)

SOLVENT	SOLUTE	RESISTIVITY Ohms-cm	REMARKS
None	Conducting Polyelectrolyte S.231-2	1×10^4	
Octoil	"		
Di Butyl Phthalate	"		Insoluble
Di Isooctyl Phthalate	"		Insoluble
Di Tridecyl Phthalate	"		Insoluble
Di Isodecyl Phthalate	"		
Tricresylphosphate	"		
Dow 200	"		
Pluracol P 410	"	2.8×10^5	polymerizes
Pluracol P 1010	"		"
Niax	"		"
HB-40	"		emulsion
PG 1200	"		"
Aroclor 1254	"		
Glycerin	" 50%	2.4×10^4	
Glycerin	" 25%	4.5×10^4	vapor pressure too high
Polyphosphoric Acid	None	30-300	
	Carbowax 20 M	1.5×10^2	
	Aluminum powder	4×10^2	
	Copper Sulfate	1×10^2	
	Aluminum Phosphate	2.8×10^2	
	DSS in stabilizer	2×10^2	vapor pressure too high

TABLE III. Effect of Lewis Acids Upon the Resistivity of Solvents

Lewis Acid	Octoil	DBP	DIDP	DIOP	DTDP
Aluminum Chloride	7×10^5	3×10^5	3×10^7	5×10^6	8×10^6
TNBAP + Aluminum Chloride	3×10^5	1×10^5			3×10^5
Aluminum Chloride + Zinc Chloride	4×10^6				
Stannous Chloride	2×10^6	1×10^6	6×10^6		4×10^6
Zinc Chloride	5×10^5	3×10^5	4×10^8		7×10^7
Antimony Pentachloride	3×10^5	1×10^4	2×10^5		4×10^5
Aluminum Bromide	1×10^7	6×10^5			
Zinc Chloride + Aluminum Bromide		3×10^5			
Zinc Chloride + Aluminum Bromide + Stannic Chloride		1×10^5			

TNBAP = tetra-N-butylammonium picrate

DIDP = diisodecyl phthalate

DTDB = dinitridecyl phthalate

DIOP = diisooctyl phthalate

Addition of organic acids and bases to solvents leads to a higher ionicity of the solution and thus greater conductivity. One inherent limiting factor in the application of these substances is their great chemical reactivity. Sulfuric acid, for example, greatly decreases the resistivity of glycerol but causes acid-catalyzed decomposition (dehydration, polymerization, etc.). In order to eliminate this difficulty, somewhat weaker organic acids have been used. Thus, polyphosphoric acid alone shows excellent conducting properties. Also, it apparently does not have an adverse effect upon solvents in which it is soluble. Among the covalent inorganic salts lithium iodide deserves especial attention. Very low resistivity has been observed for various solutions containing this solute. Thus, the resistivity of PG 1200 is reduced by 4 orders of magnitude by addition of lithium iodide to make a saturated solution.

Tetracyanoethylene and tetracyanoquinone, compounds which might be expected to capture electrons, proved unsuitable due to low solubility and instability. A "polyelectrolyte" of undisclosed chemical composition supplied by J. Ferrante, Lewis Research Center, NASA, showed good conductivity but underwent polymerization fairly readily.

5. TESTS OF PROPELLANTS AND GEOMETRIES

The tests accomplished were of two kinds: First a large number of tests were run with various propellants and various geometries to attempt to select the best propellant and optimize geometry. These tests will be reported here. Later in Chapter VI, the results of systematic tests with one propellant and one geometry will be reported.

5.1 Test Procedure

The test procedure will appear clearly from a description of a typical test which follows:

The propellant which has been vacuum refluxed is stored in a syringe which is connected to the propellant feed system. The propellant is loaded in the cylinder of the propellant feed system by the movement of the piston in the cylinder. At the end of the stroke, the connection from the syringe is closed by a stopcock, the connection from the cylinder to the propellant feed tube is open, and the direction of rotation of the synchronous motor is reversed. The nozzle is then rotated and its rotating speed is measured by means of a strobotac. The system is then operated with the high voltage off until about one-fourth of the propellant in the cylinder has been supplied to the nozzle. This period is required so as to obtain a uniform flow of the propellant to the edge of the nozzle. Once a steady flow is assumed to have taken place, the high voltage is switched on and from then on the propellant flows through the extractor to the collector, and then drips into a collecting pan. The operator can adjust the position of the extractor and the collector so as to obtain the desired focusing of the beam which is necessary so that a substantial portion of the beam goes through the windows in the collector plate. Furthermore, the operator can monitor separately the extractor, collector, and target current as well as the total current. In case the total current is not matched within 10% by the total of the currents that are monitored within the vacuum chamber, a leakage path from a part of the high voltage has to be found. This is caused, for instance, by a soiled insulating part inside or outside the vacuum chamber or by corona outside the vacuum chamber. An extractor current indicates beam interception by the extractor, which is not desired and the operator may move the extractor until the extractor current is reduced to a minimum. The two-channel recorder is utilized to monitor the indications of the Cahn balance and another variable which often is the voltage. Reading of the thrust or mass flow is accomplished as indicated in a previous chapter by measuring the difference between no accelerating voltage and full accelerating voltage on the Cahn balance. This is accomplished by switching the electrostatic generator from "on" to "standby". This procedure allows all the measurements shown in Figure 11.

From the quantities measured, one can calculate the two figures of most immediate interest: the average charge-to-mass ratio $q/m = I/\dot{m}$ and the efficiency η defined as the ratio of the power of an ideal engine of same thrust and mass flow to the actual beam power. The power is assumed here to be the product of beam current and accelerating voltage. Under these conditions the efficiency is given by

$$\eta = F^2 (2 V I \dot{m})^{-1}$$

A nomogram (Figure 19) has been devised to facilitate the calculation.

5.2 Tests with Liquid Metals

Since it has been recognized that a higher conductivity liquid is desirable as a propellant, liquid metals immediately appear attractive. One of the difficulties is of course, that they have to be maintained at a high temperature. The tests were run with an older test facility which was described in Reference 6 and is similar to the test facility described in this report except that it features a vertical disposition instead of a horizontal orientation of the beam. Tests were first run with Cerro 117, a eutectic alloy of bismuth, lead, tin, and cadmium. This alloy melts at 117°F and a temperature of 150°F was maintained in the propellant feed system by means of a heat blower. The nozzle was heated by means of several lights located inside the vacuum chamber. Similar tests were run with gallium, a pure metal which melts at 95°F. The results of these tests were disappointing inasmuch as it was extremely difficult to obtain more than a few microamperes of beam current. As these poor results did not seem compatible with the good conductivity of the metal, the lack of wettability of the nozzle material by the liquid metal was incriminated. Tentatively, the explanation for the poor results is that the metal rolls in droplets on the surface of the nozzle and that the electrical contact between the nozzle and the droplet is not sufficient to insure conduction of electric charges and charging of the droplet. To verify this hypothesis, a test was accomplished in which liquid metal was utilized to make contact between two electrodes. It was found that a rod dipped into a liquid metal made a perfect electrical contact with the liquid metal in the air but not so in a vacuum. In view of this it was decided to attempt to wet the nozzle with liquid metals, in particular gallium.

Nozzles covered with copper, then tin were used. The attempts to coat the tin nozzle with gallium were unsuccessful with various fluxes, finally even coating in an inert atmosphere failed.

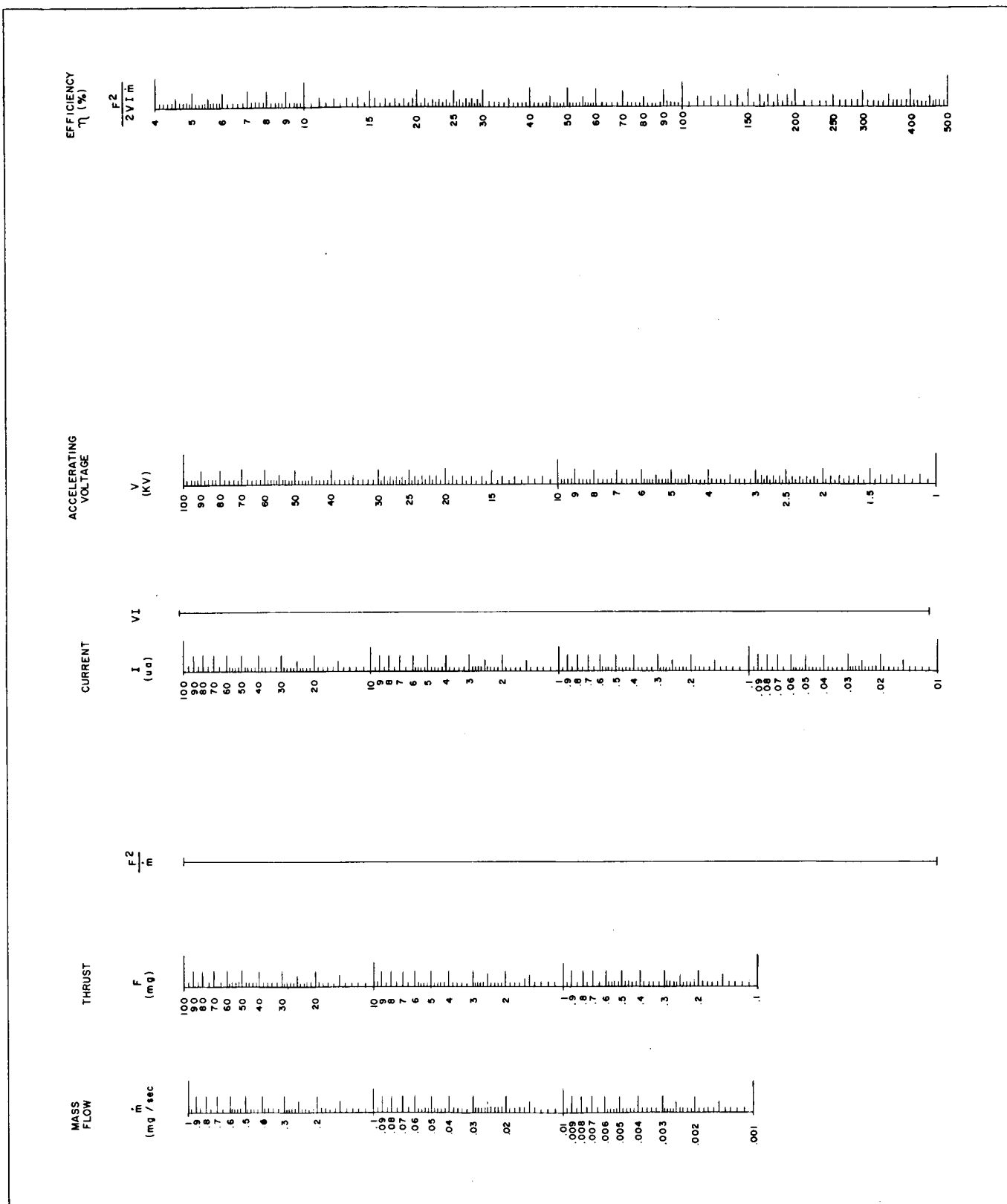


Figure 19. Nomogram for Efficiency Calculations

5.3 Tests With Organic Propellants

Figures 20 to 24 show tests accomplished with the propellants which were determined to be the most promising by virtue of their resistivity and vapor pressure. In accomplishing the tests, the voltage is raised step by step with data at every step until discharges occur in the vacuum chamber or the generator current capacity is reached. It can be seen from the curves that Octoil and Dibutylphthalate with TNBAP were the most successful propellants. Octoil + TNBAP proved to be the better propellant in that its performance was consistent in test after test: the Dibutylphthalate was erratic and for this reason, Octoil plus TNBAP was selected for the performance mapping experiments described in a later chapter.

Each experiment lasted between five minutes and one hour, depending upon the mass flow. The limiting factor was the propellant feed system which can only deliver one cylinder load at a time. The Octoil utilized during a test collects on the collector electrode in the form of a dark, viscous liquid, and then drips to the bottom of the vacuum chamber. With a continuous feed system and an adequate method of collecting the used propellant there seems to be no obstacle to the system operating for a number of hours. No wear of the nozzle or of the extractor was noticeable. On the other hand, the collector appears tarnished and etched.

The most important conclusions to be drawn from the experiments in which geometric factors were varied are that the system performance with the 10° nozzle is slightly better than with the other nozzles and that the external or ring extractor results in a charge-to-mass ratio double that obtained with the center extractor.

With Octoil + TNBAP a charge-to-mass ratio as high as 180 coul/kg was often obtained and charge-to-mass ratios higher than 100 coul/kg were consistently obtained. The efficiency calculated from the thrust measurements was most consistently between 65% and 90%.

5.4 Tests With Polyphosphoric Acid

Polyphosphoric Acid, $H_3PO_4 \times P_2O_5$, has a vapor pressure compatible with the system and a lower resistivity than any other propellant tried to date. The acid has one major disadvantage in that it attacks aluminum. New collector and extractor electrodes of stainless steel were made and a plate to prevent splashing back of the nozzle was installed between the nozzle and the nozzle support (Figure 7). The test results are shown on Figures 25 and 26 and seem to indicate a charge-to-mass ratio of the order of 500 coul/kg, however, this data is not confirmed by thrust measurements and the efficiency is unknown. Difficulties were encountered

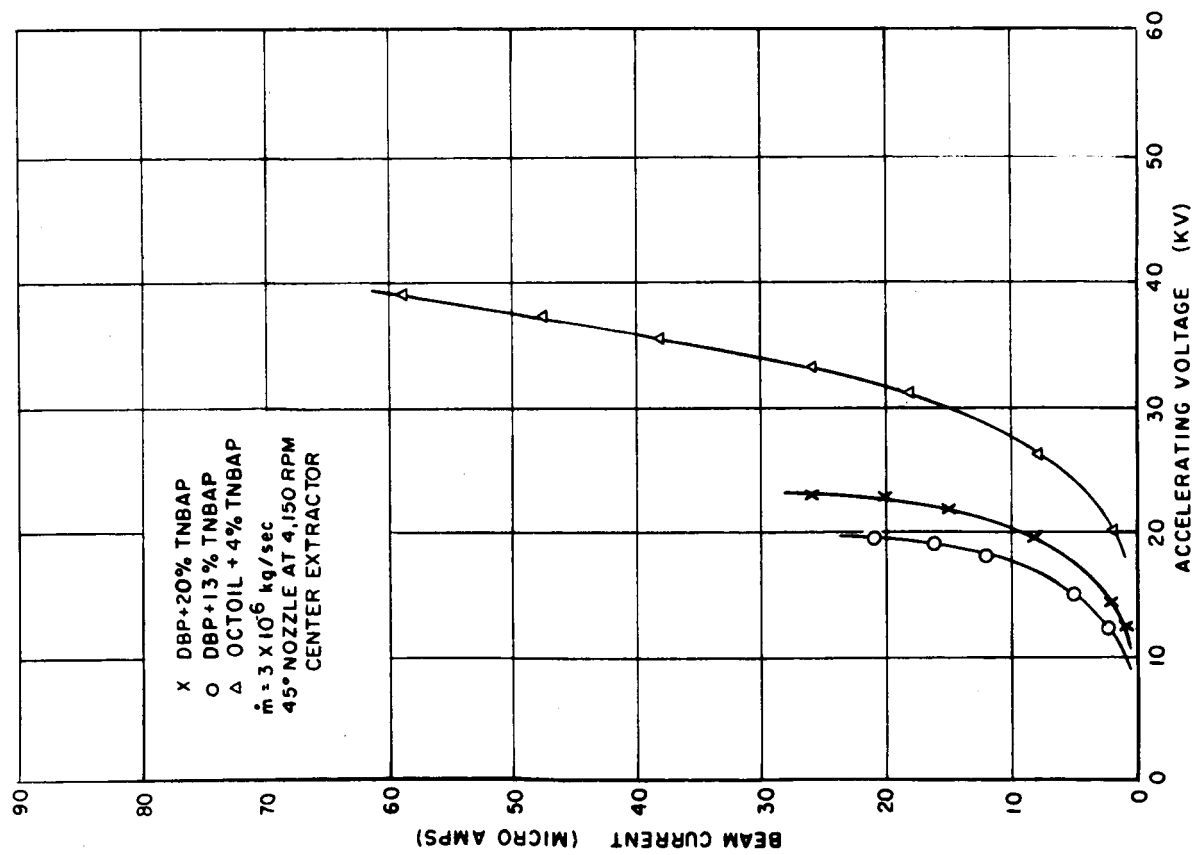


Figure 20. Propellant Tests, Beam Current vs. Accelerating Voltage

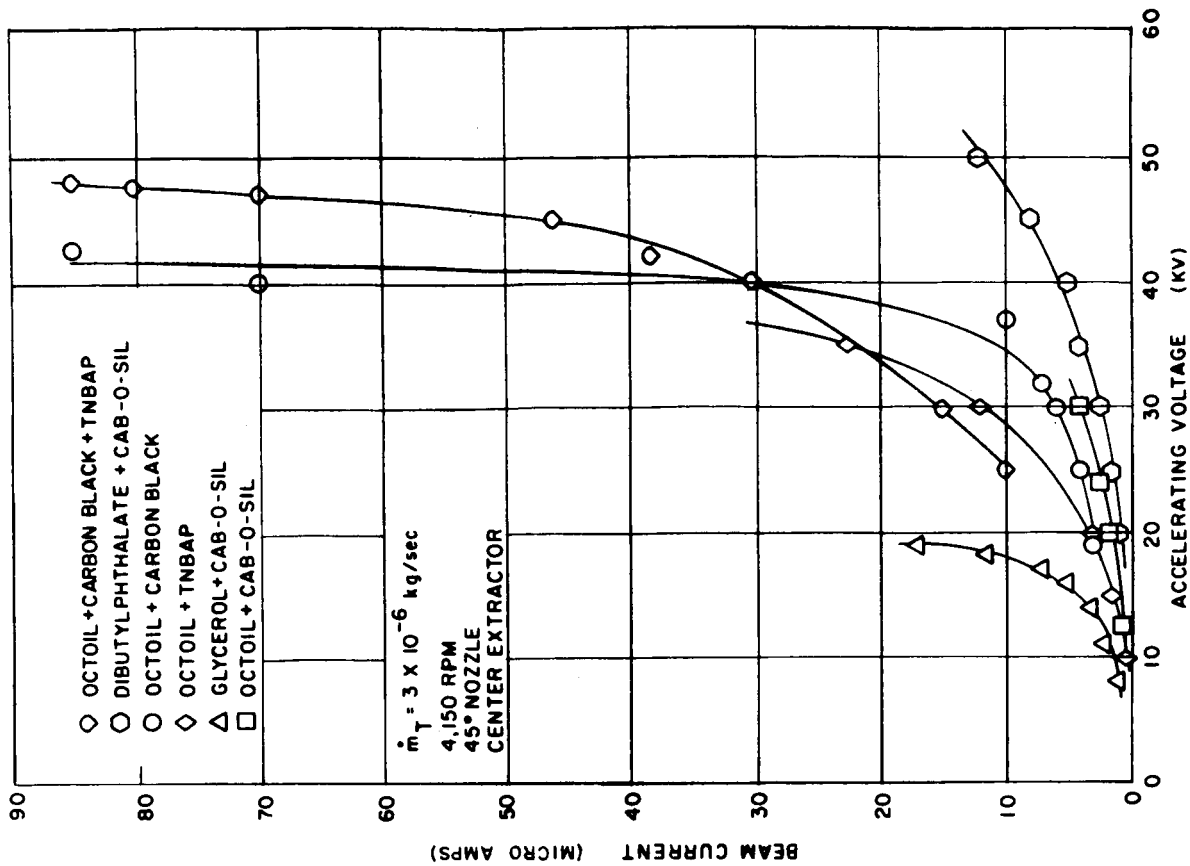


Figure 21. Propellant Tests, Beam Current vs. Accelerating Voltage

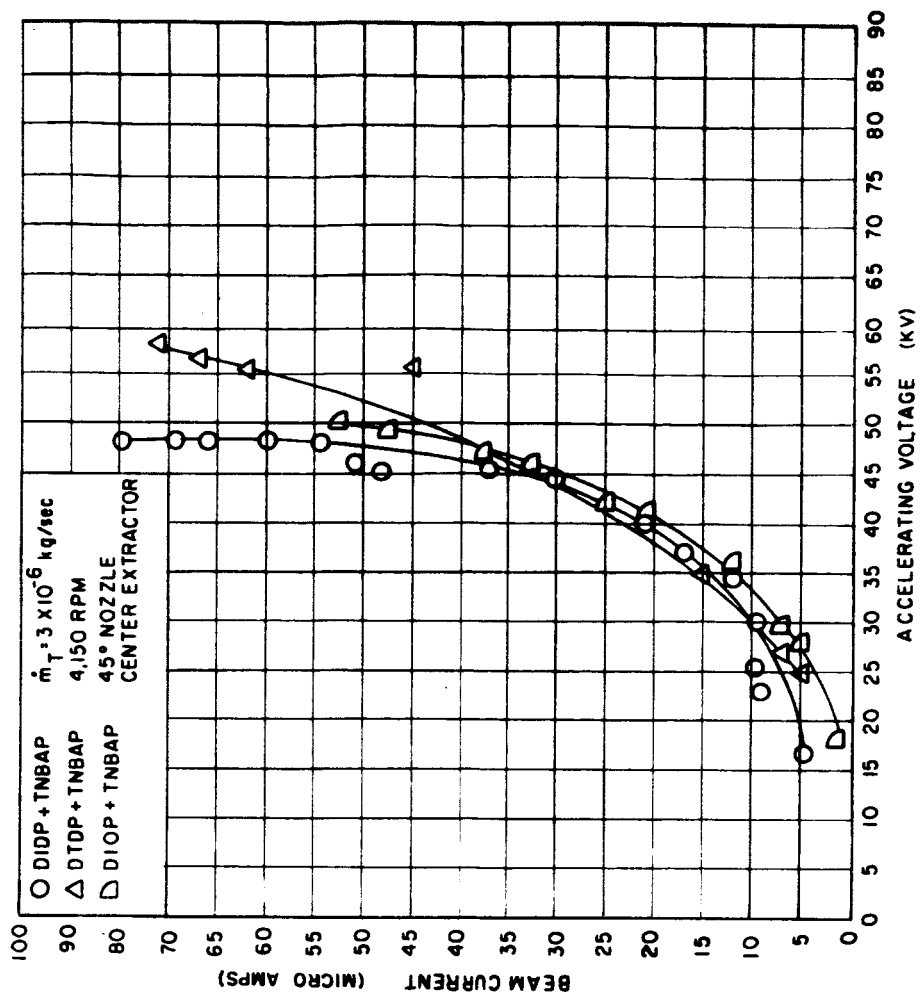


Figure 22. Propellant Tests, Beam Current vs. Accelerating Voltage

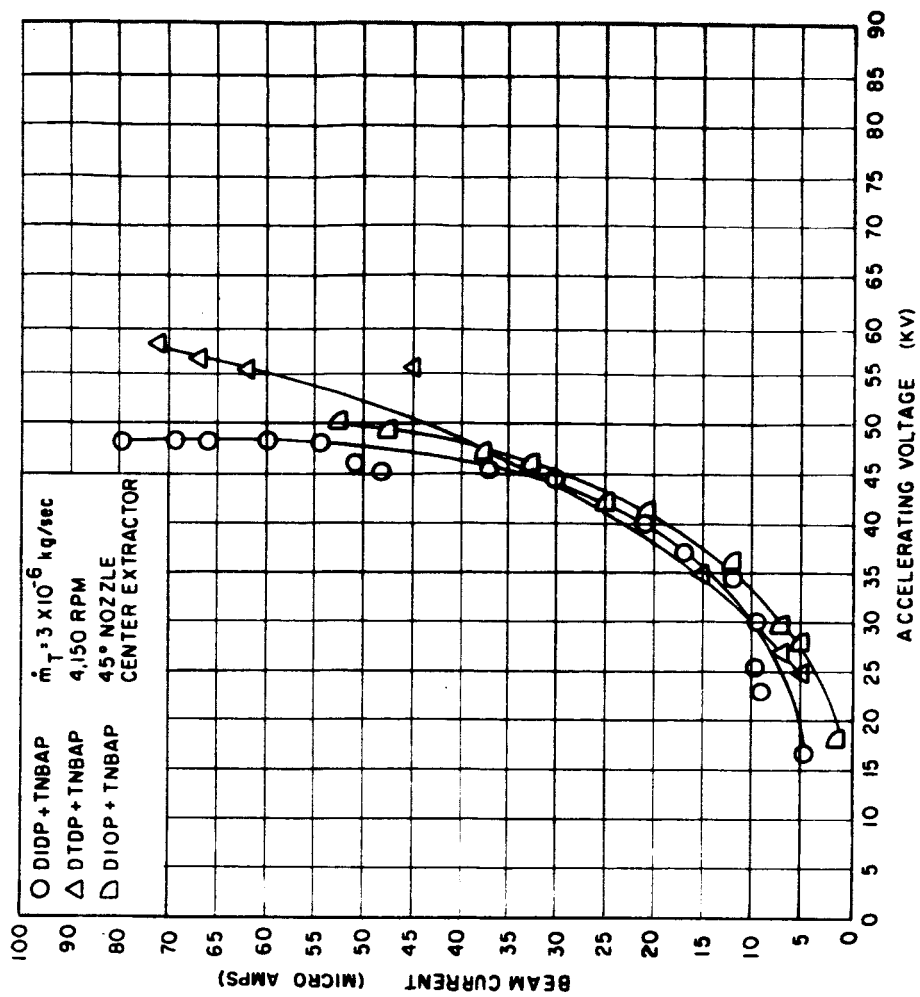


Figure 23. Propellant Tests, Beam Current vs. Accelerating Voltage

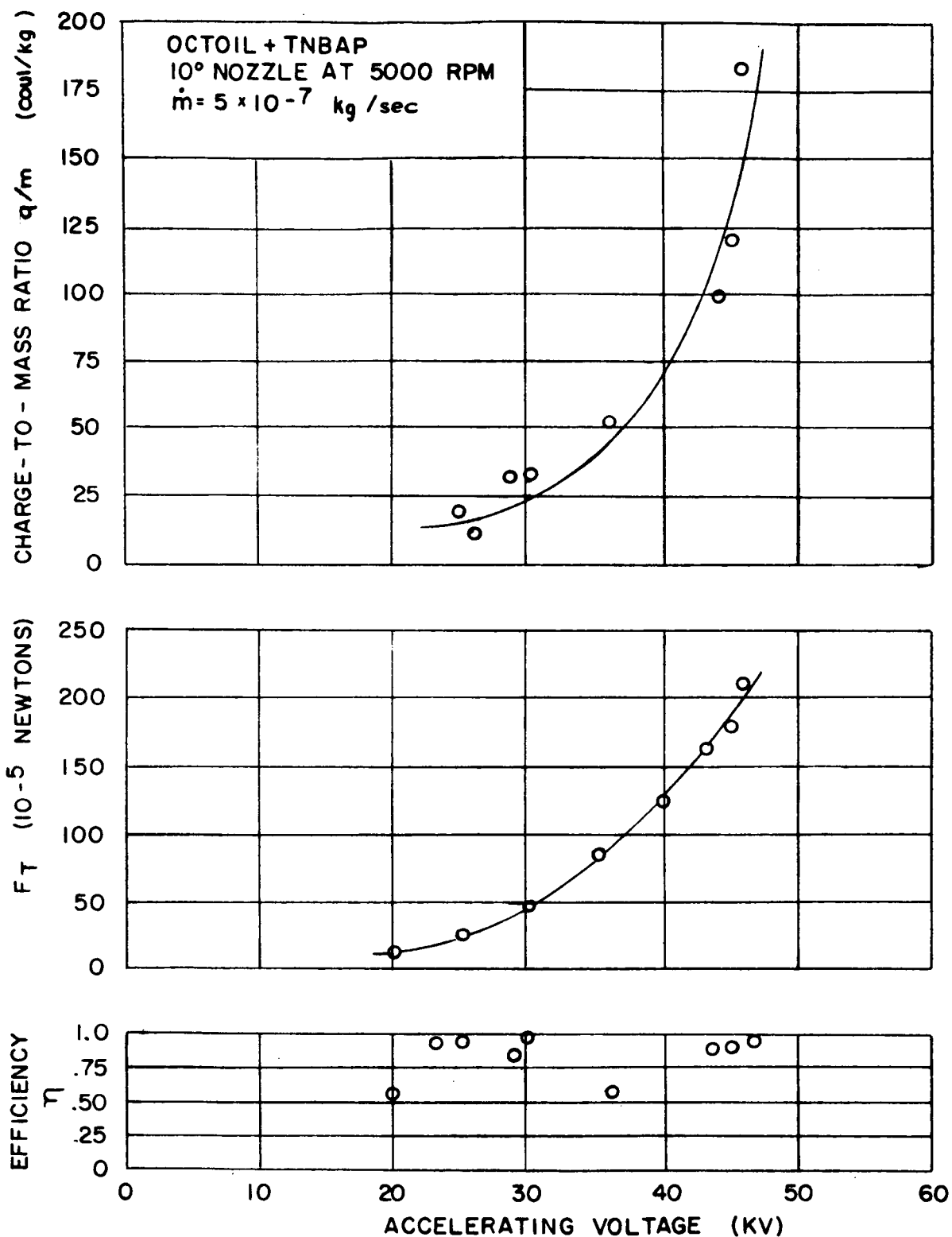


Figure 24. Average Charge-to-Mass Ratio (q/m), Total Thrust per Mass Flow (F_T/\dot{m}) and Efficiency (η) vs. Accelerating Voltage

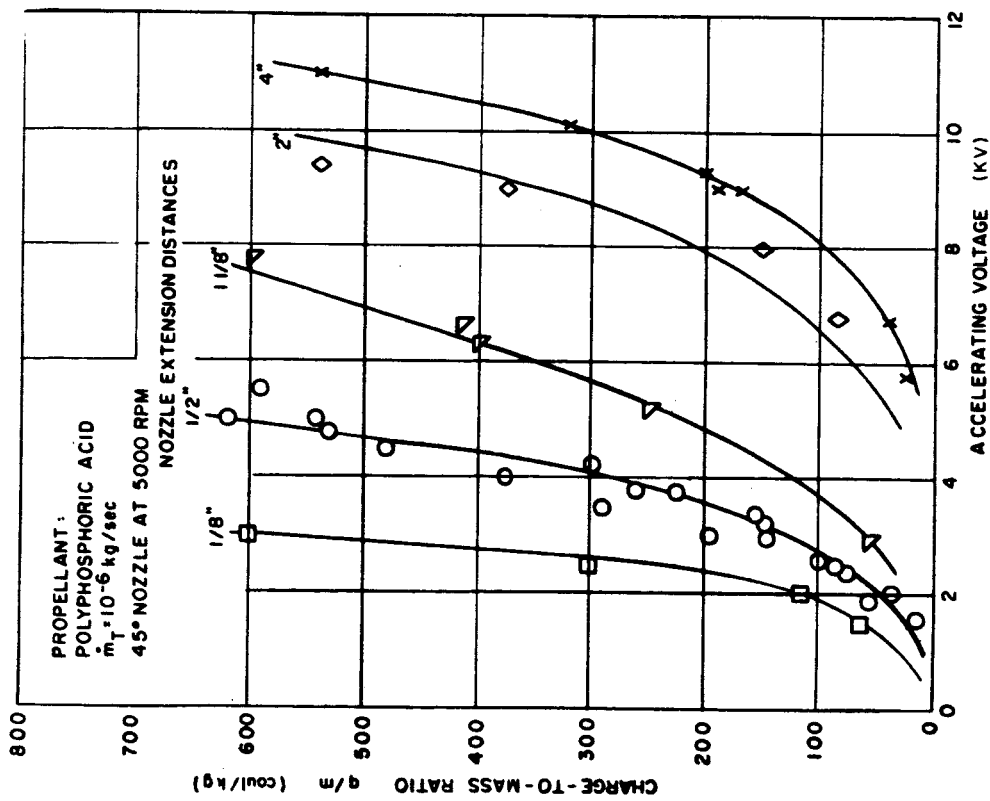


Figure 25. Average Charge-to-Mass Ratio vs. Accelerating Voltage for Various Nozzle-Extractor Distances

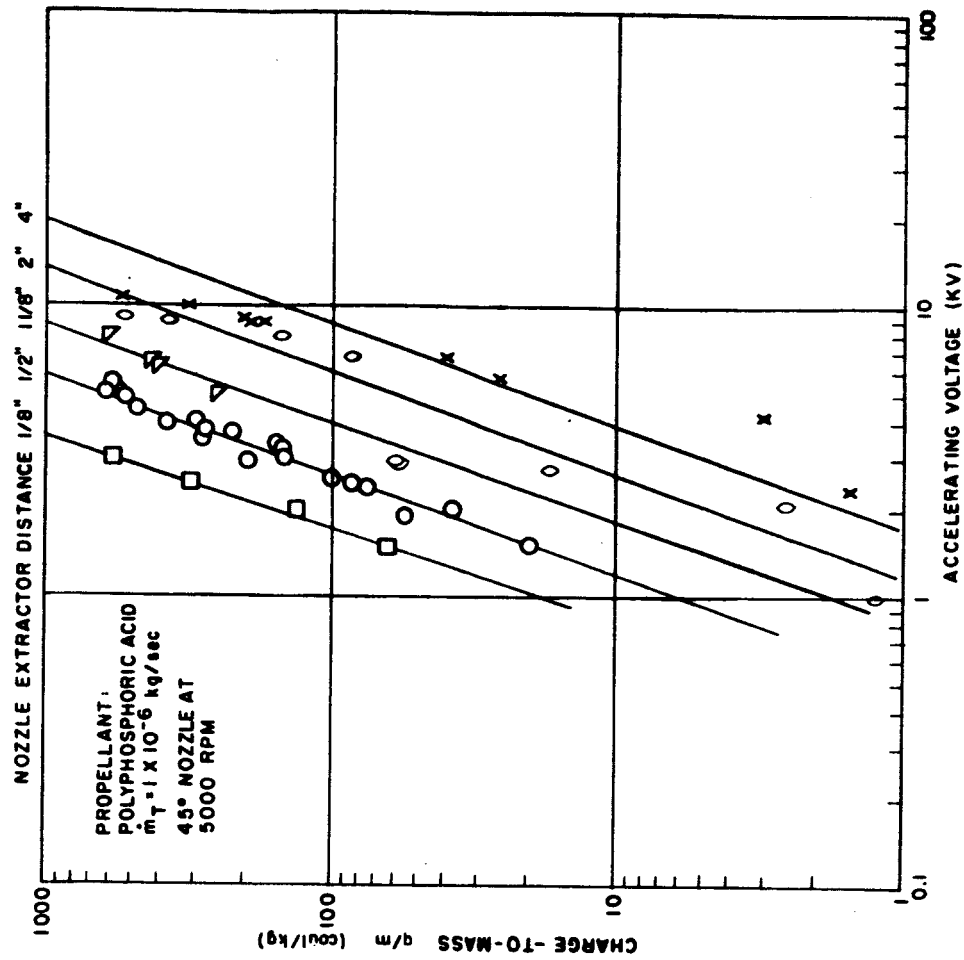


Figure 26. Average Charge-to-Mass Ratio vs. Accelerating Voltage for Various Nozzle-Extractor Distances

during the tests for the reason that the polyphosphoric acid is very hygroscopic and tends to decompose and release P_2O_5 .

5.5 Tests with Massenfilter

As pointed out earlier, it is difficult to determine what is the effect of the massenfilter orientation with respect to the beam. The method utilized here consisted of aiming the quadrupole with the rail voltage off so as to maximize the current on the target. The orientation so obtained was maintained during the test. A typical curve obtained is shown on Figure 27 and shows a peak of charge-to-mass ratio at 80 coul/kg. It is felt that this curve should be interpreted with caution, since it is not confirmed by thrust measurements.

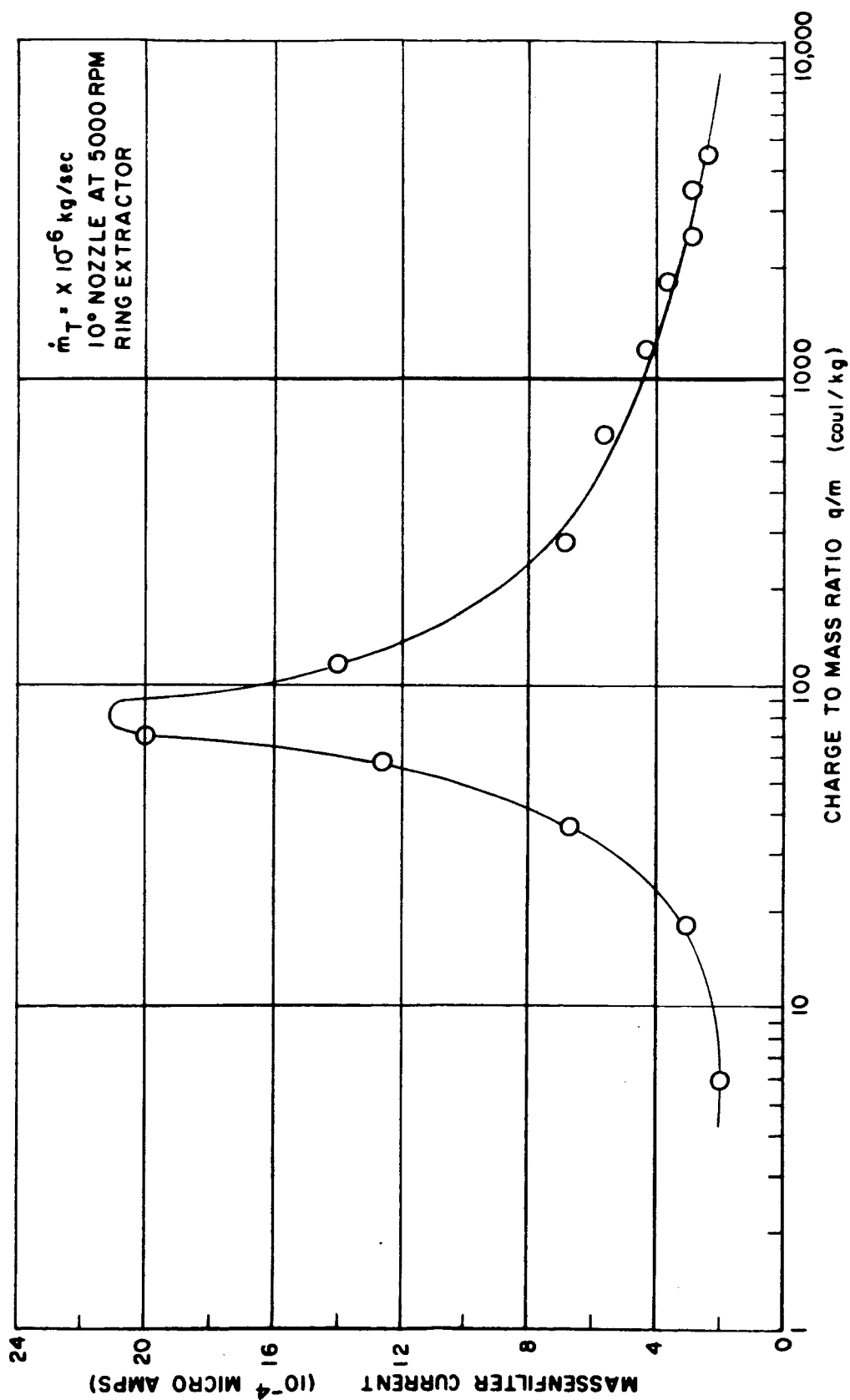


Figure 27. Massenfilter Current vs. Charge-to-Mass Ratios (Resolution = 110)

6. RESULTS AND INTERPRETATION OF PERFORMANCE MAPPING EXPERIMENTS

In order to provide the systematic data required for empirical determination of trends and for theoretical interpretation, a series of performance mapping experiments was carried out. In these experiments, the propellant and geometry were kept fixed and the mass flow rate, nozzle rotating speed, and voltage were varied. The propellant was Octoil with 4% TNBAP. The geometry corresponded to a 10^0 aluminum nozzle with the optimal annular extractor electrode located 1 cm from the nozzle and the collector electrode located some 6 cm in front of the nozzle. Mass flow rates of 0.5, 3, 15×10^{-6} kg/sec, rotating speeds of 1, 5, 12×10^3 rpm, and a range of voltages between roughly 20 and 40 kilovolts were used. Standard instrumentation as described above was employed to monitor the controlled variables (i.e., \dot{m}_T , ω , V) and to measure collector current, I_C , target current, I_t , and target thrust, F_t . Because of difficulties in obtaining reliable direct measurements of the target mass flow, \dot{m}_t , this quantity was taken to be I_t/I_C \dot{m}_T .

With this propellant and geometry, we have

$$\gamma = 2.7 \times 10^{-2} \text{ kg/sec}^2$$

$$\epsilon = \epsilon_0 = 8.85 \times 10^{-12} \text{ farad/m}$$

$$\nu = 5.2 \times 10^{-5} \text{ m}^2/\text{sec}$$

$$\rho_m = 9.8 \times 10^2 \text{ kg/m}^3$$

$$\sigma = 5 \times 10^{-4} \text{ mho/m}$$

$$L = 10^{-2} \text{ m}$$

$$r/L = 4.29$$

Therefore, with units for \dot{m} , ω and V of 10^{-6} kg/sec, 1.05×10^2 rad/sec ($= 10^3$ rpm), and 10^4 volts, respectively, we have, from Section 3, above

$$I_1 = 7.9 \times 10^{-10} V \dot{m}^{2/3} \omega^{2/3} [1 - \exp(-\sigma\tau/\epsilon)] C_1 D^{1/3} \text{ amp}$$

$$F_1 = 4.0 \times 10^{-6} V \dot{m}^{5/6} \omega^{1/3} [1 - \exp(-\sigma\tau/\epsilon)]^{1/2} (C_1 D^{1/3})^{1/2} \text{ N}$$

$$I_3 = 3.0 \times 10^{-12} V^3 \dot{m} [1 - \exp(-\sigma\tau/\epsilon)]^2 C_3^3 \text{ amp}$$

$$\begin{aligned}
F_3 &= 2.4 \times 10^{-7} V^2 \dot{m} [1 - \exp(-\sigma\tau/\epsilon)] C_3^{3/2} N \\
I^* &= 1.1 \times 10^{-7} V^3 \dot{m}^{-1/3} \omega^{-4/3} (B K_4^2)^2 D^{-2/3} \text{ amp} \\
F^* &= 4.6 \times 10^{-5} V^2 \dot{m}^{1/3} \omega^{-2/3} B K_4^2 D^{-1/3} N \\
\lambda &= 5.8 \times 10^{-3} V^{-2} \dot{m} \omega^2 [1 - \exp(-\sigma\tau/\epsilon)] C_1 D / B K_4^2 \\
\Gamma &= 1.5 \times 10 V^{-1} \dot{m}^{-1/6} \omega^{1/3} [1 - \exp(-\sigma\tau/\epsilon)]^{-1/2} (C_1 D^{1/3} / C_3^3)^{1/2} \\
\mu &= 3.0 \times 10^{-2} \dot{m}^{4/9} \omega^{4/9} [1 - \exp(-\sigma\tau/\epsilon)]^{2/3} C_3 D^{2/9} / (B K_4^2)^{2/3}
\end{aligned}$$

where $I_1 (F_1)$, $I_3 (F_3)$, $I^* (F^*)$ are the beam current (thrust) in the weak space-charge limit of the extraction mode, in the weak space-charge limit of the disintegration mode, and in the strong space-charge limit of both modes, respectively, and λ , Γ , μ are dimensionless parameters specifying the space-charge effects. We have from Section 3, that, in general,

$$\begin{aligned}
I &= \begin{aligned} &I_1 g_1(\lambda) && \lambda > \lambda^* \equiv f_1(\Gamma) \\ &I_3 [g_3(\mu)]^3 = I_3 [q_3(\lambda^{1/3}/\Gamma^{2/3})]^3 && \lambda < \lambda^* \equiv f_1(\Gamma) \end{aligned}
\end{aligned}$$

and the analogous expression for F . It will be recalled that the dimensionless parameter D is of order 1 while $C_1 \approx C_3 \approx K_4 \gg 1$.

The theory developed in Section 3 assumes that the charge-to-mass ratio is uniform, i.e., that the efficiency $\eta \equiv P^2/2 V \dot{m} I$ is 1. Since the actual measured efficiencies are not 1, the data must be smoothed in order for comparisons with predicted behavior to be meaningful. This smoothing is carried out by defining equivalent current, I_{eq} , and equivalent thrust, F_{eq} , as

$$I_{eq} = I_{meas} / \eta_{meas}$$

$$F_{eq} = F_{meas} / \eta_{meas}$$

where the subscript "meas" denotes measured values. It is trivial to verify that the equivalent efficiency, $\eta_{eq} \equiv F_{eq}^2/2 V \dot{m} I_{eq} \equiv 1$ and that the smoothed data are thereby compatible with the theory. The performance mapping data to be discussed in this section are all presented in this smoothed, "equivalent" form.

Although there is no reason a priori to expect the data to conform to any of the three limiting cases discussed above, it is instructive to consider the three possibilities. To this end, Figures 28, 29, and 30 display equivalent collector current, target current and target thrust respectively, as functions of voltage for a rotating speed of 5×10^3 rpm and the three total mass flow rates of 0.5, 3, 15×10^{-6} kg/sec. For ease of interpretation, straight lines corresponding to a V^3 (V^2) dependence have been drawn through the three families of current (thrust) data points. It is clear that the data follow these power-laws much more closely than a linear law; therefore, the conjecture that these data correspond to the weak space-charge limit of the extraction mode is untenable. Moreover, the fact that the currents increase, rather than decrease, with increasing mass flow rate is counter to the predicted decrease of current with mass flow in the strong space-charge limit.

Further evidence that the system is not operating in the strong space-charge limit is presented in Figures 31, 32, and 33 which display equivalent collector current, target current, and target thrust, respectively, as functions of voltage for a total mass flow rate of 0.5×10^{-6} kg/sec and the three rotating speeds of 1, 5, 12×10^3 rpm. Again straight lines corresponding to a V^3 (V^2) law have been drawn through the current (thrust) data points and, again, these power laws are seen to be a reasonable fit of the data. Moreover, the data exhibit little, if any, dependence upon rotating speed. Thus the data are consistent with operation in the weak space-charge limit of the disintegration mode, rather than in the strong space-charge limit with its predicted decrease in current and thrust with increasing rotating speed. The net effect of Figures 28 through 33 is therefore to i) rule out operation in either the weak space-charge limit of the extraction mode or the strong space-charge limit and ii) leave open the possibility of operation in the weak space-charge limit of the disintegration mode.

Since the data are consistent with the predicted voltage dependence in the weak space-charge limit of the D mode, we now consider the dependence upon rotating speed and mass flow rate. To this end, Figures 34 and 35 display equivalent target current and thrust, respectively, as functions of rotating speed for a total mass flow rate of 3×10^{-6} kg/sec and voltages of 24, 30 and 34 kilovolts. Clearly, these data are consistent with the predicted independence of current and thrust with rotating speed. This independence is further illustrated in Figures 36 and 37 which display equivalent target current and thrust as functions of target mass flow rate for a voltage of 20 kilovolts and the three rotating speeds of 1, 5, 12×10^3 rpm. Moreover, the straight lines which have been drawn through the data to display a linear variation with mass flow rate are clearly consistent with

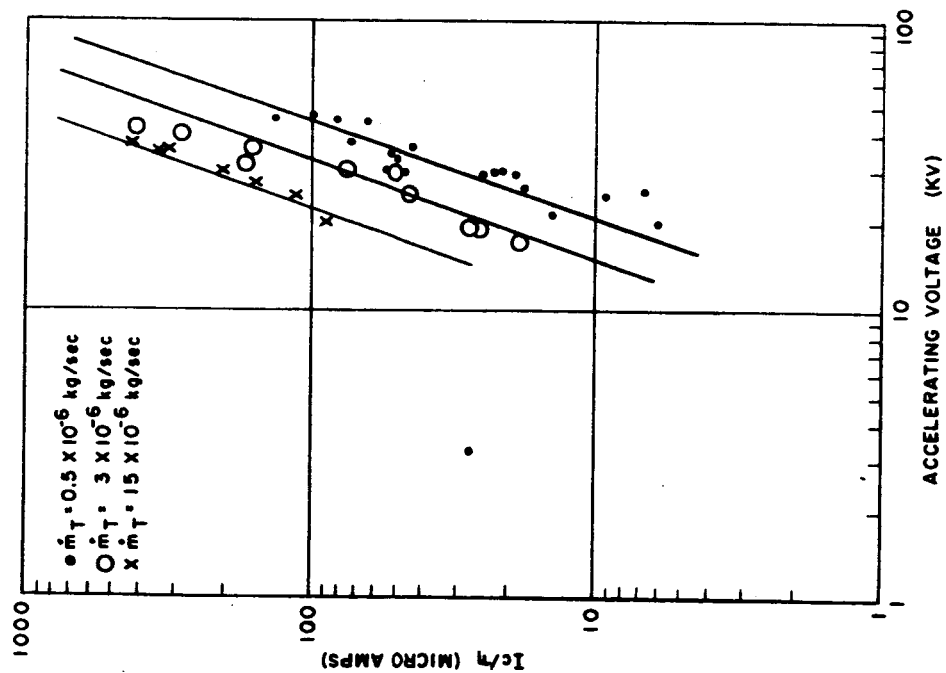


Figure 28. Equivalent Collector Current vs. Voltage for a Rotating Speed of 5,000 rpm and Total Mass Flow Rates of 0.5 , 3 , & 15×10^{-6} kg/sec

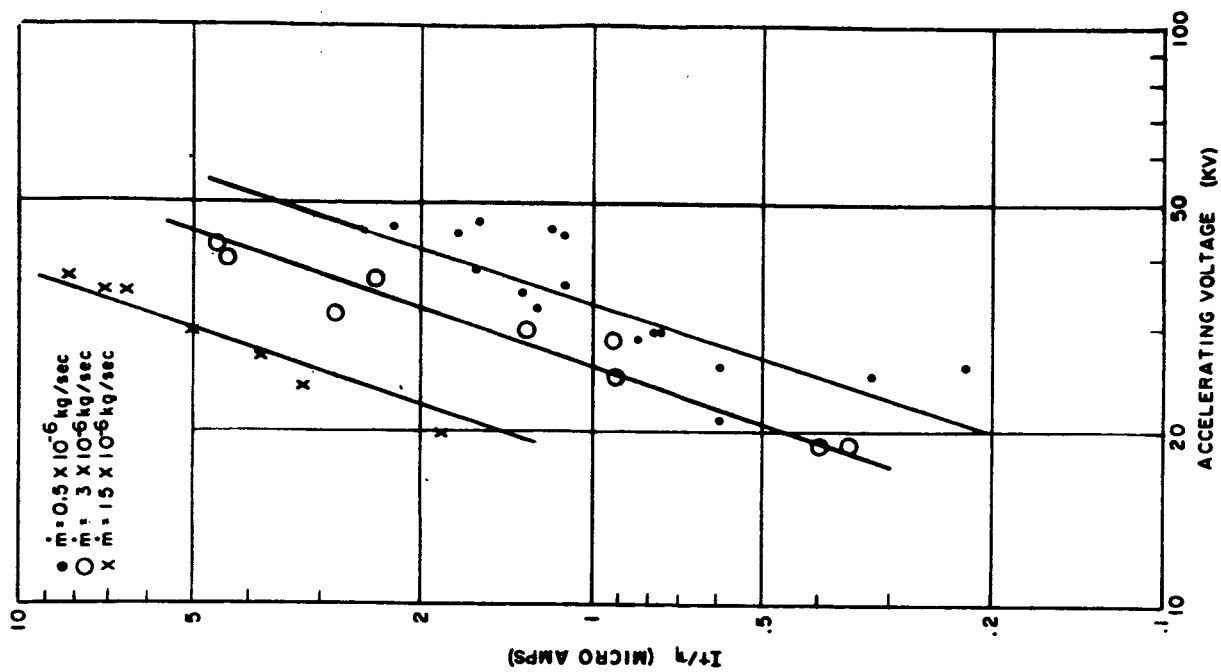


Figure 29. Equivalent Target Current vs. Voltage for a Rotating Speed of 5,000 rpm and Total Mass Flow Rates of 0.5 , 3 , & 15×10^{-6} kg/sec

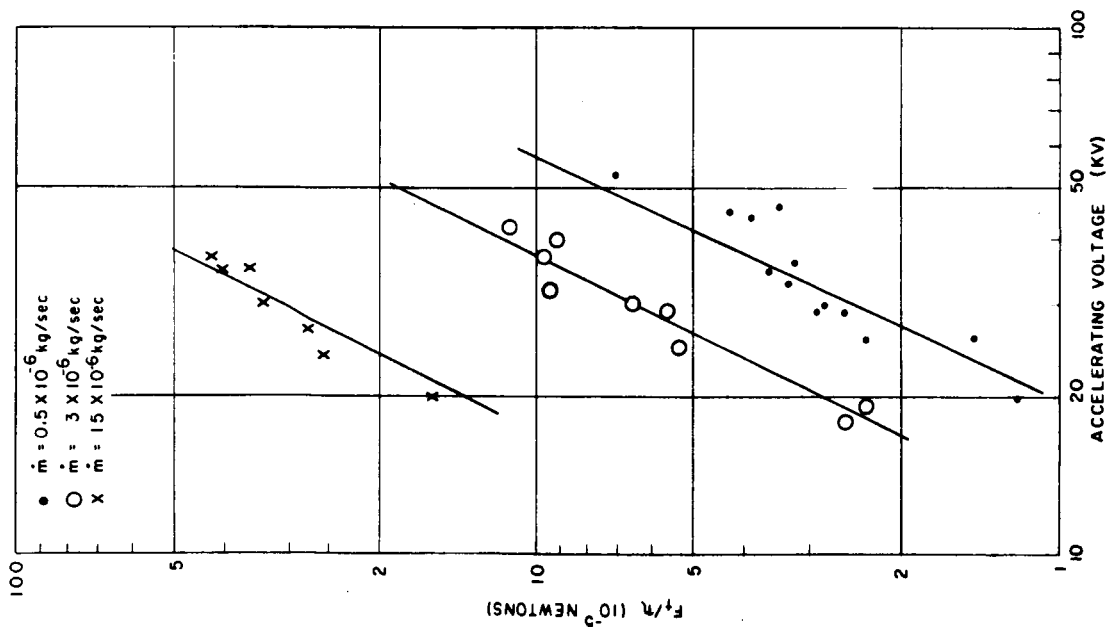


Figure 30. Equivalent Target Thrust vs. Voltage for a Rotating Speed of 5,000 rpm and Total Mass Flow Rates of 0.5 , 3 , & 15×10^{-6} kg/sec

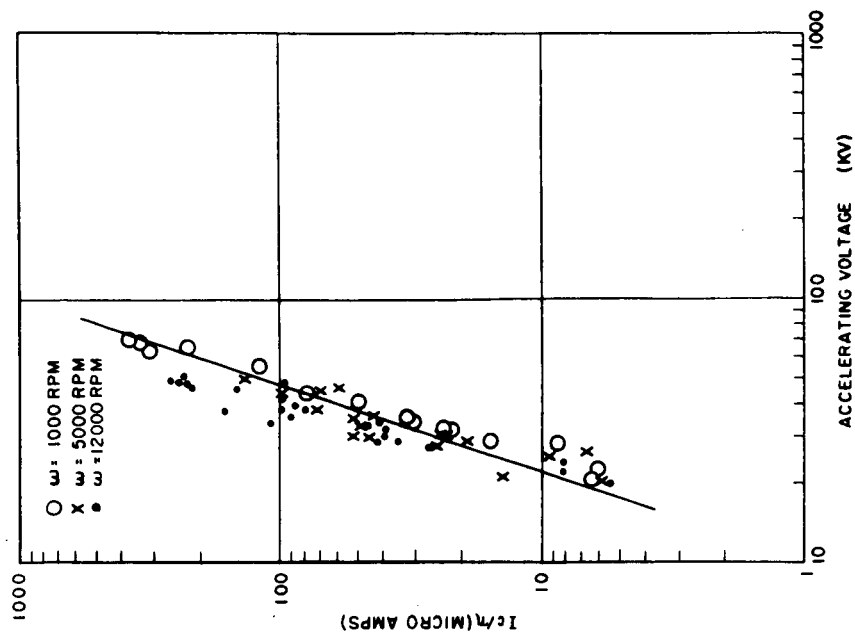


Figure 31. Equivalent Collector Current vs. Voltage for a Total Mass Flow of 0.5×10^{-6} kg/sec and Rotating Speeds of 1,000, 5,000 and 12,000 rpm

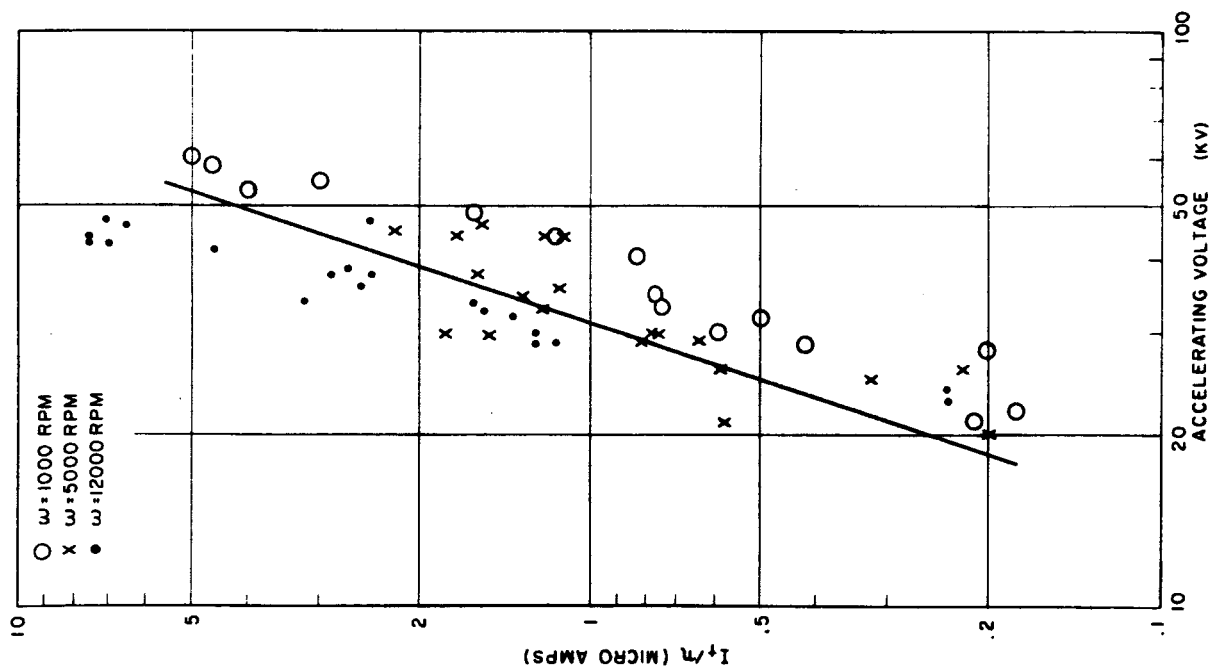


Figure 32. Equivalent Target Current vs. Voltage for a Total Mass Flow of 0.5×10^{-6} kg/sec and Rotating Speeds of 1,000, 5,000 and 12,000 rpm

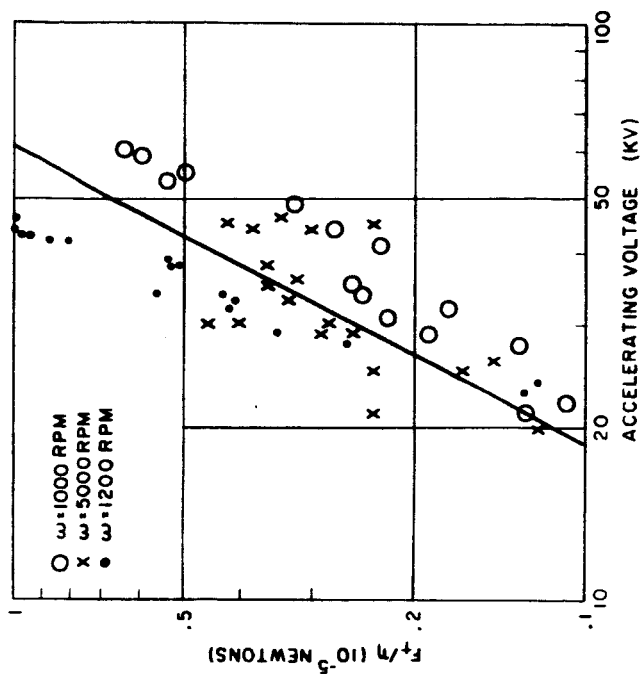


Figure 33. Equivalent Target Thrust vs. Voltage for a Total Mass Flow of 0.5×10^{-6} kg/sec and Rotating Speeds of 1,000, 5,000 and 12,000 rpm

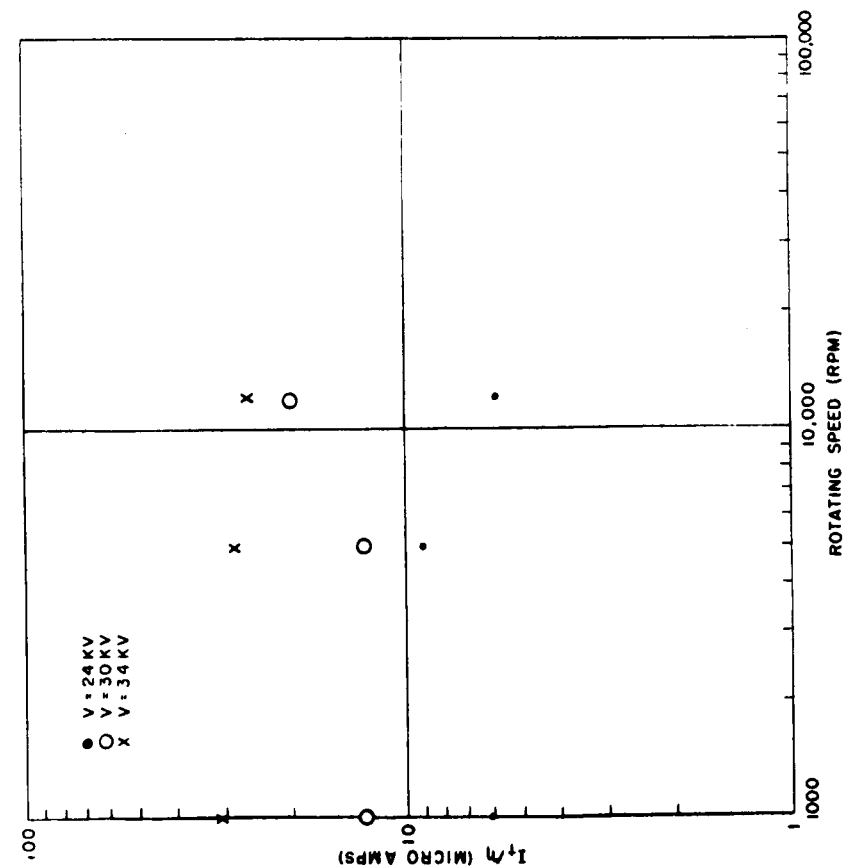


Figure 34. Equivalent Target Current vs.
Rotating Speed for a Total Mass
Flow Rate of 3×10^{-6} kg/sec
and Voltage of 24, 30, & 34 KV

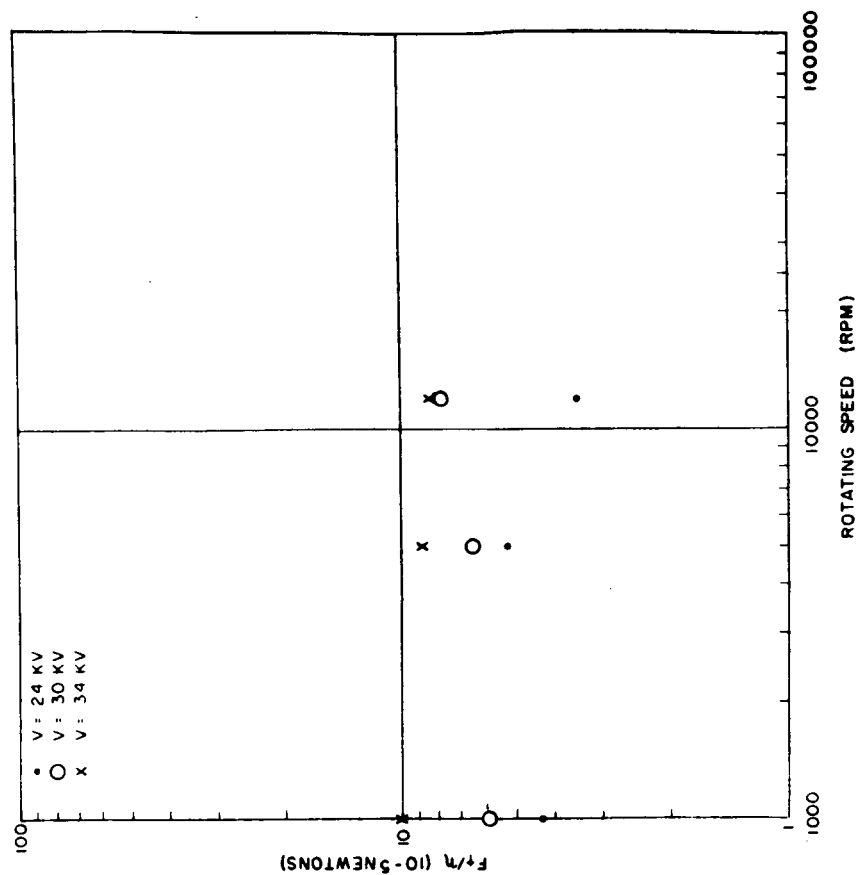


Figure 35. Equivalent Target Thrust vs.
Rotating Speed for a Total Mass
Flow Rate of 3×10^{-6} kg/sec
and Voltage of 24, 30, & 34 KV

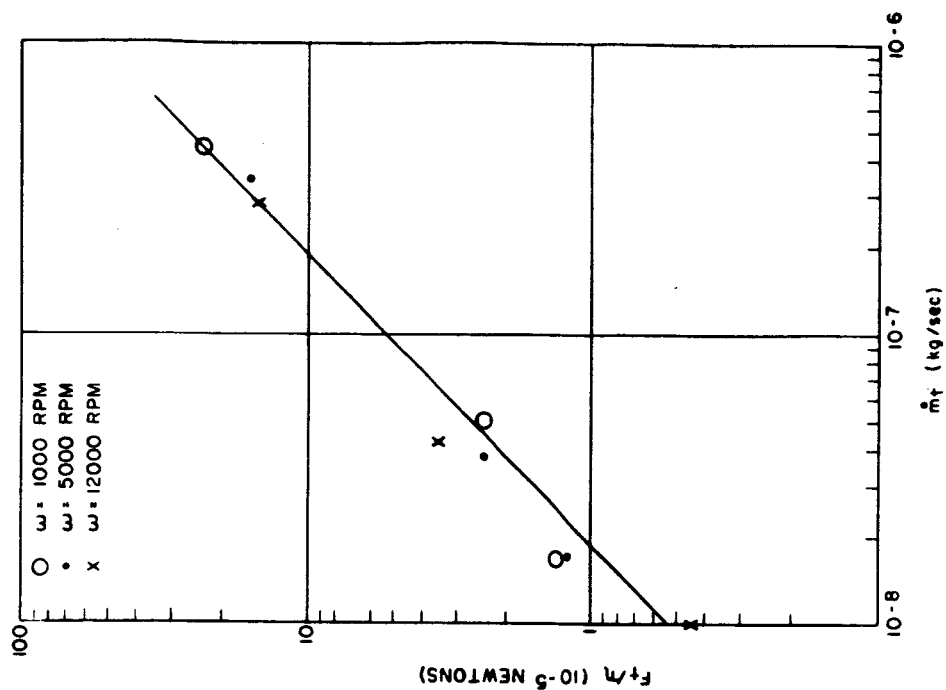


Figure 36. Equivalent Target Current vs. Target Mass Flow Rate for a Voltage of 20 KV and Rotating Speeds of 1,000, 5,000 and 12,000 rpm

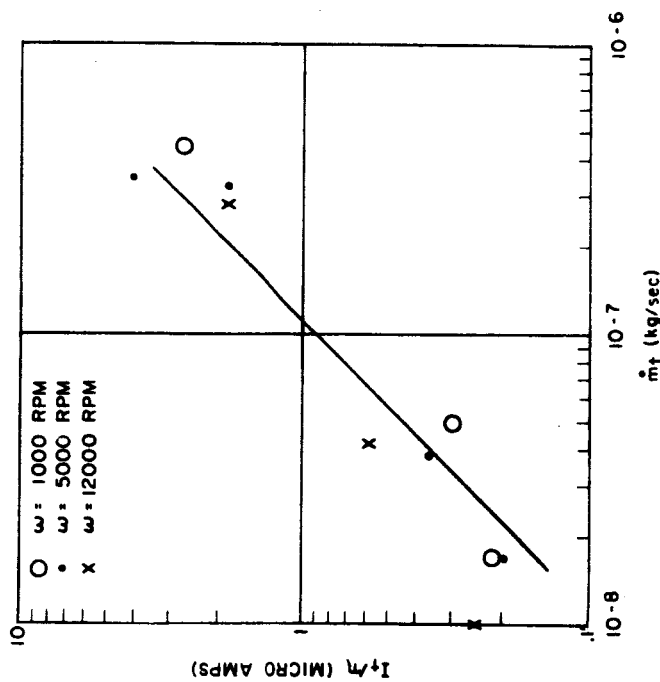


Figure 37. Equivalent Target Thrust vs. Target Mass Flow Rate for a Voltage of 20 KV and Rotating Speeds of 1,000, 5,000 and 12,000 rpm

the data. This linear variation with mass flow rate is also exhibited in Figure 38, which displays equivalent target thrust as a function of target mass flow rate for a rotating speed of 5×10^3 rpm and the three voltages of 20, 30, and 37 kilovolts.

Thus the data presented in Figures 28 through 38 exhibit trends with \dot{m} , ω , and V which are consistent with operation in the weak space-charge limit of the disintegration mode. It remains to be demonstrated that the data are consistent with the values of λ , μ , and Γ required for such operation. In order to estimate values of these parameters, it is necessary estimate the term $[1 - \exp(-\sigma\tau/\epsilon)]$. We shall underestimate this term by taking

$$\frac{\sigma\tau}{\epsilon} \sim \frac{\sigma}{\epsilon} \frac{a}{\omega} = 10 \quad \frac{a}{\omega} \quad \begin{array}{l} a \text{ in microns} \\ \omega \text{ in } 10^3 \text{ rpm} \end{array}$$

Figure 39 shows the Raleigh-limit charge-to-mass ratio of Octoil droplets as a function of droplet size. For the range of charge-to-mass ratios obtained in these experiments, approximately $10^{-1} \mu$ is a lower bound on droplet size. Therefore

$$\frac{\sigma\tau}{\epsilon} > \frac{1}{\omega} > 0.1$$

Consequently,

$$[1 - \exp(-\sigma\tau/\epsilon)] > 0.1$$

Thus the term $[1 - \exp(-\sigma\tau/\epsilon)]$ is of order 1 and does not vary by more than an order of magnitude during the performance mapping experiments. Taking this term to be 1 and assuming operation in the weak space-charge limit of the D modes permits C_3 to be evaluated, since

$$I = I_3 = 3.0 \times 10^{-12} V^3 \dot{m} C_3^3 \text{ amp}$$

For example, from Figure 30, $I = 6.6 \times 10^{-5}$ amp for $V = 40$ kilovolts and $\dot{m} = 0.5 \times 10^{-6}$ kg/sec. Thus

$$C_3^3 = \frac{6.6 \times 10^{-5}}{(3 \times 10^{-12})^3 (4)^3 (0.5)} = 0.7 \times 10^6$$

$$C_3 = 90 \approx 10^2$$

Moreover, since $C_1 \approx C_3 \approx K_4$, we have $C_1 \approx 10^2$, $K_4 \approx 10^2$. Under the plausible assumption that B is of order 1, substitution into the expressions above gives

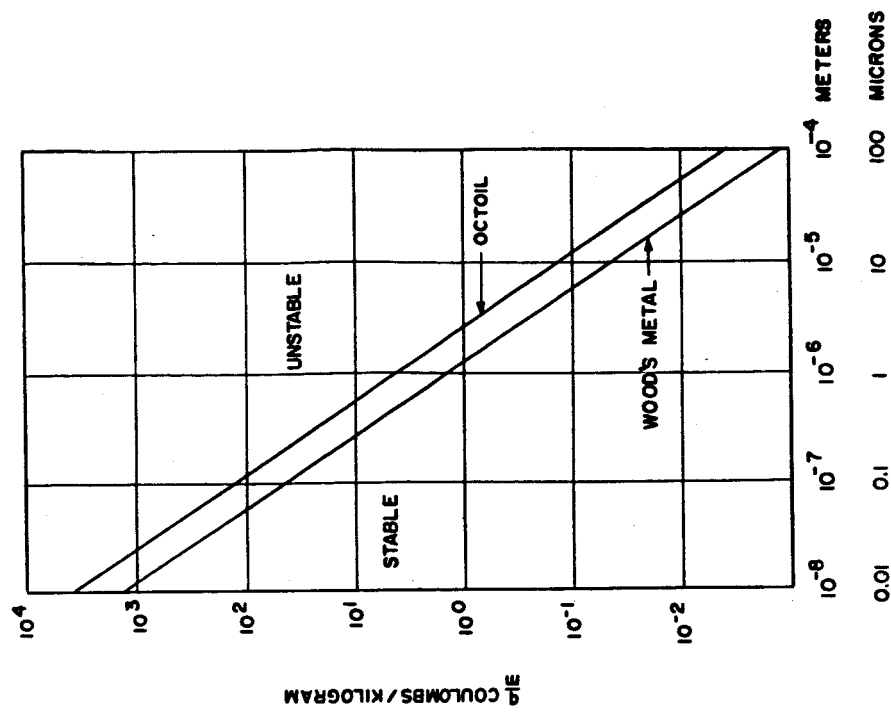


Figure 39. Rayleigh Maximum Specific Charge as a Function of Drop Sizes

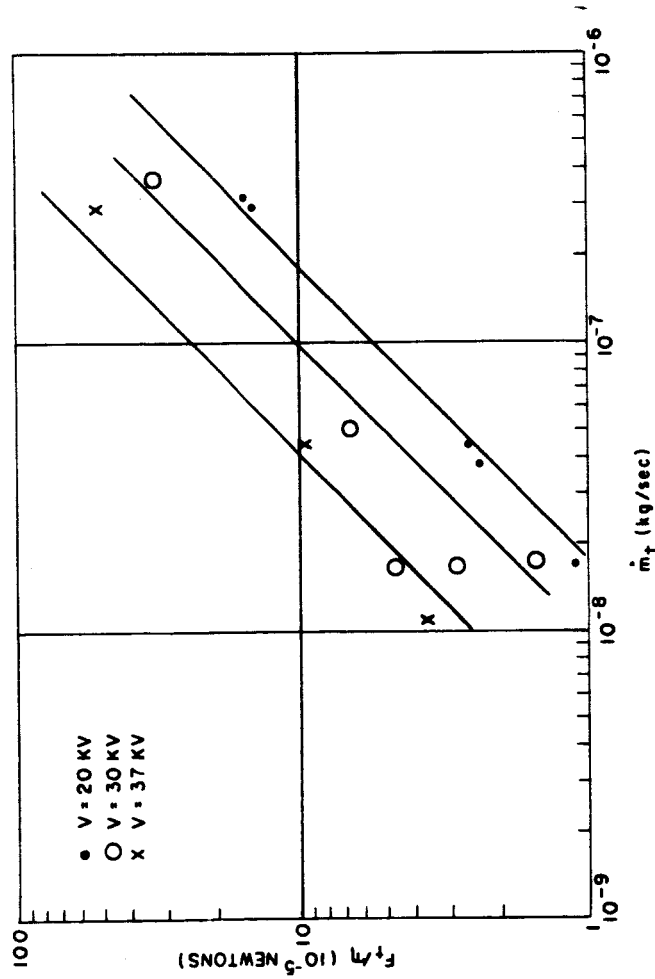


Figure 38. Equivalent Target Thrust vs. Target Mass Flow Rate for a Rotating Speed of 5,000 rpm and Voltage of 20, 30, 37 KV

$$\begin{aligned}\lambda &\approx 5.8 \times 10^{-9} & V^{-2} \dot{m} \omega^2 \\ \Gamma &\approx 1.5 \times 10^{-1} & V^{-1} \dot{m}^{-1/6} \omega^{1/3} \\ \mu &\approx 6 \times 10^{-3} & \dot{m}^{4/9} \omega^{4/9}\end{aligned}$$

In order for the performance mapping data to correspond to the weak space-charge limit of the disintegration mode, it is necessary that

$$\begin{aligned}\Gamma &< 1 \\ \lambda &< f_1(\Gamma) < \Gamma^{-1} \\ \mu &<< 1\end{aligned}$$

It is readily seen that these conditions are satisfied for all the data points in the performance mapping experiments.

In summary, then, a series of performance mapping experiments was carried out, in which \dot{m} , ω , and V were varied by factors of 30, 12, and 2.5 respectively, resulting in variations of the space charge parameters λ and Γ by factors of 3×10^4 and 10, respectively. The current and thrust data obtained thereby exhibit trends with \dot{m} , ω , V which are consistent with operation in the weak space-charge limit of the disintegration mode. Moreover, a posteriori estimation of the dimensionless parameters appearing in the general theory permits such operation to be reconciled quantitatively with the requirements of the theory.

7. CONCLUSIONS AND RECOMMENDATIONS

The test facility with a horizontal beam configuration has proven adequate for the tests of the system with the first acceleration stage.

The tests run using Octoil and a salt as propellant have provided repeatable test data. The low conductivity of Octoil is responsible for the yet relatively low charge-to-mass ratio obtained, of the order of 100 coulombs/kilogram. A liquid of higher conductivity, with a low vapor pressure must be found in order to obtain higher values of the charge-to-mass ratio. It is to be noted that the same conclusion is reached by experimenters using needles (Ref. 4, page 38) when several needles are used in parallel for several hours (a needle is capable of a mass flow equal to one hundredth of the lowest mass flow possible with the rotating nozzle).

The analytical investigation has defined the characteristics required of the ideal propellant, low density, high viscosity, low surface tension and high conductivity in addition to the operating requirement of low vapor pressure. The theoretical relationship between the performance parameters and the controllable elements fits remarkably well with the experimental data. The chemical investigations have uncovered those classes of compounds and mixtures which are the most likely to meet the desired propellant characteristics. The values of thrust and mass flow reached during the experiment were limited by the propellant feed system and not by any inherent characteristics of the system.

Improvements in efficiency are expected to be realized from a more steady mass flow. Current measured efficiency is in the range of 60% to 90% and appears independent of the specific impulse. Future tests should be primarily concerned with variations of the propellant, long duration tests and the operation with several stages of acceleration.

REFERENCES

1. William R. Mickelsen and Harold R. Kaufman, "Electrostatic Thrusters for Space Propulsion, Present and Future", NASA Lewis Research Center, British Interplanetary Society Symposium on Advanced Propulsion Systems, London, England, October 1963.
2. Ernst Stuhlinger, "Ion Propulsion for Space Flight", McGraw-Hill Book Company, New York, 1964.
3. D. B. Langmuir, et al, Patent No. 2,880,337, "Particle Acceleration Method and Apparatus", March 31, 1959.
4. E. Cohen, "Research on Charged Colloid Generation", APL TDR 64-75, June 1964.
5. D. Gignoux, H. F. Anton, and J. J. Shea, "Charged Colloid Generating System for Electric Propulsion", NASA CR-54049, October 1963.
6. D. Gignoux, H. F. Anton, H. Einbinder, "Nozzle for Colloidal Propulsion, Analytical Investigation", Final Report NASr-45, August 1961.
7. D. Gignoux, "Electrostatic Generators in Space Power Systems", AIAA Paper No. 64-450, 1st AIAA Annual Meeting, Washington, D. C., June 1964.
8. W. Paul and M. Raether, "Das elektrische Massenfilter", Zeitschrift für Physik, Bd. 140, S. 262-273 (1955).
9. W. Paul, H. P. Reinhard and U. von Zahn, "Das elektrische Massenfilter als Massenspektrometer und Isotopentrenner", Zeitschrift für Physik, Bd. 152, S. 143-182 (1958).
10. I. E. Dayton, F. C. Shoemaker, and R. F. Mozley, Rev. Sci. Inst. 25, 485 (1954).
11. N. W. McLachlan, "Theory and Application of Mathieu Functions", Clarendon Press, Oxford, pp. 40 and 98.
12. J. W. Cahn, Phys. Fluids 5, 1662 (1962).
13. W. K. H. Panofsky and M. Philips, Classical Electricity and Magnetism (Addison-Wesley Publishing Co., Inc., Reading, Mass. 1962).
14. David L. Lockwood, William Mickelsen, and Vladimir Hamza, "Analytic Space-Charge Flow and Theoretical Electrostatic Rocket Engine Performance", American Rocket Society, Electric Propulsion Conference, March 1962.

FINAL REPORT DISTRIBUTION LIST

CONTRACT NAS3-4106

<u>Addressee</u>	<u>Number of Copies</u>
1. NASA Headquarters FOB - 10B 600 Independence Avenue, S. W. Washington, D. C. 20546 Attention: RNT/James Lazar	2
2. NASA-Lewis Research Center Spacecraft Technology Division Cleveland, Ohio 44135 Attention: J. H. Childs	2
3. NASA-Lewis Research Center Space Technology Division 21000 Brookpark Road Cleveland, Ohio 44135 Attention: J. Ferrante	5
4. NASA-Lewis Research Center Spacecraft Technology Procurement Section 21000 Brookpark Road Cleveland, Ohio 44135 Attention: John H. DeFord	1
5. NASA-Lewis Research Center 21000 Brookpark Road Cleveland, Ohio 44135 Attention: Technology Utilization Office	1
6. NASA-Lewis Research Center 21000 Brookpark Road Cleveland, Ohio 44135 Attention: Reports Control Office	1
7. Commander Aeronautical Systems Division Wright-Patterson Air Force Base, Ohio Attention: AFAPL (APIE)/Mr. Robert Supp	1

	<u>Addressee</u>	<u>Number of Copies</u>
8.	NASA-Lewis Research Center 21000 Brookpark Road Cleveland, Ohio 44135 Attention: Library	2
9.	NASA-Lewis Research Center 21000 Brookpark Road Cleveland, Ohio 44135 Attention: C. T. Norgren	2
10.	NASA-Marshall Space Flight Center Huntsville, Alabama Attention: (M-RP-DIR)/E. Stuhlinger	1
11.	NASA Scientific and Technical Information Facility Box 5700 Bethesda 14, Maryland Attention: RQT-2448/NASA Representative	6
12.	Rocketdyne Division of North American Aviation, Inc. Electric Propulsion Section Canoga Park, California Attention: Dr. J. F. Hon	1
13.	Rocket Power, Inc. 3016 East Foothill Boulevard Pasadena, California Attention: Dr. S. Singer	1
14.	Ion Physics Corporation Burlington, Massachusetts Attention: Dr. Sam Nablo	1
15.	Astrosystems, Inc. 82 Naylor Avenue Livingston, New Jersey Attention: Mr. R. E. Wiech, Jr.	1
16.	Space Technology Laboratories, Inc. Physical Research Laboratories 8433 Fallbrook Avenue Canoga Park, California Attention: Dr. D. B. Langmuir	1

	<u>Addressee</u>	<u>Number of Copies</u>
17.	Reaction Motors Division Thiokol Chemical Corporation Denville, New Jersey Attention: Dr. Wilby Courtney	1
18.	Aerojet-General Nucleonics P. O. Box 77 San Ramon, California Attention: Dr. John Luce	1
19.	Gruman Aircraft Engineering Corporation Bethpage, Long Island New York Attention: Mr. Paul Grinoch	1
20.	Hughes Research Laboratories 3011 Malibu Canyon Road Malibu, California Attention: Dr. Ron Knechtli	1
21.	Electro-Optical Sysytems, Inc. 300 North Halstead Street Pasadena, California Attention: Dr. A. T. Forrester	1
22.	The Martin Company P. O. Box 5837 Orlando, Florida Attention: Engineering Library MP 30	1
23.	AFWL Kirtland Air Force Base, New Mexico Attention: WLPC/Capt. C. F. Ellis	1
24.	Aerospace Corporation P. O. Box 95085 Los Angeles, California 90045 Attention: Library Technical Documents Group	1
25.	Westinghouse Astronuclear Labs. Pittsburgh, Pennsylvania 15234 Attention: H. W. Szymanowski, Mgr. Electrical Propulsion Lab.	1

	<u>Addressee</u>	<u>Number of Copies</u>
26.	NASA-Lewis Research Center 21000 Brookpark Road Cleveland, Ohio 44135 Attention: Edward A. Richley Mail Steop 301-1	1
27.	NASA-Lewis Research Center 21000 Brookpark Road Cleveland, Ohio 44135 Attention: W. R. Mickelsen M. S. 301-1	1

ABSTRACT

A charged colloid generating system adaptable to an electrostatic thruster has been developed. The liquid forms a thin film inside a rotating nozzle and charged droplets are pulled off the edge by an electric field. A test facility has been built instrumented by a thrust measuring balance and a quadrupole mass spectrometer. An analytical investigation has been accomplished relating the performance parameters to the variables controlled by the operator. Analytical and experimental values are compared. A chemical investigation has been initiated with the aim of finding better propellants. The test data is given in several charts.